Annual Report

Project Title: Roadmap: Technologies for Cost Effective, Spatial Resource Assessments for Offshore Renewable Energy

Covering Period: 1 October 2011 to 30 September 2012

Date of Report: 28 October 2012

Recipient: University of Massachusetts Dartmouth

Award Number: M10PC00096

Working Partners, Project Managers and Principal Investigator:

University of Massachusetts Dartmouth MREC
John Miller, Project Manager, j2miller@umassd.edu, 508.999.6732
Woods Hole Oceanographic Institution
Dr. Eugene Terray, Technical Lead, eterray@whoi.edu, 774.392.0070
University of Massachusetts Dartmouth SMAST
Brian Howes, PI, bhowesr@umassd.edu, 508.910.6316
University of Massachusetts Amherst
Dr. J. D. McGowan, jgmcgowa@ecs.umass.edu, 413.545.2756 |
University of Hawaii
Dr. Pierre Flement, PI, pierre@soest.hawaii.edu (808) 956-6663
University of Washington
Dr. William Plant, PI, plant1944@gmail.com, 206.543.7836
Battelle Memorial Institute, Inc.
Paul Dragos, dragosp@battelle.org,
Imaging Science Research
Dr. Dennis Trizna, dennis@isr-sensing.com, 703.801.1417
Ocean Server
Robert Anderson, anderson@ocean-server.com, 508.678.0550
Teledyne RD instruments
Jerry Mullison, jmullison@teledyne.com, 858.842.2600

BOEMRE Project Team: Contracting Officer – Lisa Algarin
Contracting Administrator – Joanne Murphy
Contracting Officer's Representative – Angel McCoy

Background

It has been estimated that the energy in the oceans (Offshore wind, waves and tides) could provide all of the world's demand for electricity, but many challenges must be met prior to realizing even a small fraction of that potential. One of the challenges is the ability to sense, measure at a distance, the resources and their surrounding environments. Today the standard is to place fixed structure in the ocean or to have people physically visit a location to do assessments. This is unacceptable for two reasons:

1) Cost – The costs of a ocean metrological (Met) tower is on the order of $1 million and on site surveys are man power intensive, but establishing the potential resource and the status of surrounding habitats requires this information.

2) Spatial Information – Current techniques provide point or, at most, linear measurements. With a need for assessment that starts at the sea sub-bottom and goes to the top of marine atmospheric surface boundary layer and might cover hundreds of square miles, new technologies are needed to measure resource variations over proposed development areas and to provide the varied levels of forecasting needed for grid and device operators.

The New England Marine Renewable Energy Center (MREC) proposed to develop a Roadmap for Cost Effective, Spatial Resource Assessments for Offshore Renewable Energy under a National Ocean Partnership Program (NOPP) solicitation, M10PS00152. To accomplish this broad scope of work MREC assembled a team of leading researchers from four Universities: Universities of Massachusetts Dartmouth (UMD), Massachusetts Amherst (UMA), Hawaii (UH), and Washington (UW); the Woods Hole Oceanographic Institution (WHOI); and three companies: Battelle Memorial Institute (BMI), Imaging Sciences Research (ISR), and Teledyne RDI (TRDI). The team is led by John Miller, UMD, Project Lead, and Dr. Eugene Terray, WHOI, Technical Lead.

Remote sensing can be best viewed from the distance to area under assessment:

Long Range, HF phase array radar provided by ISR and UH.

Task 2. Statistical characterization of winds, waves and currents over large area.
Potential to assess wind, waves and currents at range of several hundred km.
Test ability to measure large areas and to forecast conditions for grid operators.

Intermediate Range, microwave radar provided by ISR and UW.

Task 3. High resolution, spatial imaging of wind, waves, currents, and bathymetry
Potential to provide high resolution assessments of wind, wave and currents.
Test ability to provide detailed mapping for device siteing and extreme conditions.

Short Range, Surveys and testing by UMA, UMD and TRDI.

Task 1. High resolution wind profiling from buoys and small boats, UMA
Potential to replace fixed Met tower with floating LIDAR or SODAR.
Survey current manufacturers and assess potential capability.

Task 5. Surveys of the sub-bottom, bottom sediment, and benthic biotic communities using automated underwater vehicles (AUVs), UMD
Potential to reduce sampling or improve area coverage using sensors on AUVs
Test optical and acoustic sensors mounted on AUVs to determine capability.

Task 4, Mapping of currents and waves using Doppler sonar, TRDI
Potential for more effective siteing and monitoring conditions to tuning systems
Testing and data analysis for beam width and orientation, and turbulence statistics

Results

The program met most of its goals in 2012. Tasks 1 (Wind profiling), 3 (Intermediate range radar), 4 (Sonar for siteing and monitoring) and 5 (Physical survey techniques) experienced some delays primarily due to weather issues, but completed their research tasks. Task 1 and 4 have submitted draft reports, and drafts for 3 and 5 are being written. Editing of the drafts and development of the integrated roadmap is progressing.

The one significant performance deficiency has been in Task 2 (Long range radar). This task has significant potential for providing remote monitoring and, perhaps more importantly, forecasting for utilities using marine renewable energy. A key component of this task will be a side by side test of radars from the University of Hawaii and ISR. However, a critical component of the Hawaii radar, was not delivered and a new source had to be located. This is not a common part and has a long lead time. The result was a delay in the build of the radar and the testing, and the need for no cost extensions to the contract (see schedule Attachment 1). Testing is now schedule for early 2013 and the contract scheduled to end September 30th 2013.

Specific comments by task follow:

Task 1. High resolution wind profiling from buoys and small boats.

The overall objective of this study was a detailed technical based review (with all corresponding open source references) of the available technologies and current state-of-the-art of instrumentation systems for the measurement of offshore winds- with an emphasis on utility scale power generation wind farms. In the introduction/background section of the report, the review covered Sodar, LIDAR, and other potential measuring systems (balloons, remote sensing vehicles). Following this work, it was concluded that the scope of this report would be limited to SODAR and LIDAR based wind data acquisition systems. In the next section the principles of operation of both these systems were summarized along with a detailed review of past wind resource measurements and

their current commercial status (including a summary of instrument specifications and power source requirements). The next section of the report presents a summary of potential offshore-sited platforms for wind resource assessment. The potential designs of a number of manufacturers were summarized and were divided into fixed and floating platforms. The fixed platform category included long and short-term platforms, nearby islands, and retasking an existing offshore platform. Next, four floating platform systems are reviewed (SeaZephir, AXYS WindSentinel, FliDAR, and Fugro). A final conclusions/recommendations section presents a summary of our current opinions on the subject. At this time, we concluded that LIDAR systems were technically superior to SODAR systems, with reservations about their relatively high costs. Problems with day-to-day operation and power requirements of measurement systems are pointed out. For floating systems, the need for stable platforms or motion compensating software was also discussed. Furthermore, the rapid commercial development and corresponding offshore wind measurements standards development will require constant monitoring of technical developments in this area of instrumentation.

Task 2. . Statistical characterization of winds, waves and currents over large area.
This task has two efforts, University of Hawaii and ISR. ISR has continued its work accomplishing all tasks except for the side by side testing with the Hawaii radar. Comments on both efforts follow:

ISR: ISR has continued development of its radar with several recent noteworthy accomplishments:

a. *New miniaturized narrow band loop receive antenna construction*
8 miniaturized capacitor-tunable loop antennas were built, housed in 6-inch PVC pipe for weather protection. A photo of the 8 elements is shown below in Figure 1a, with four gain responses at right.

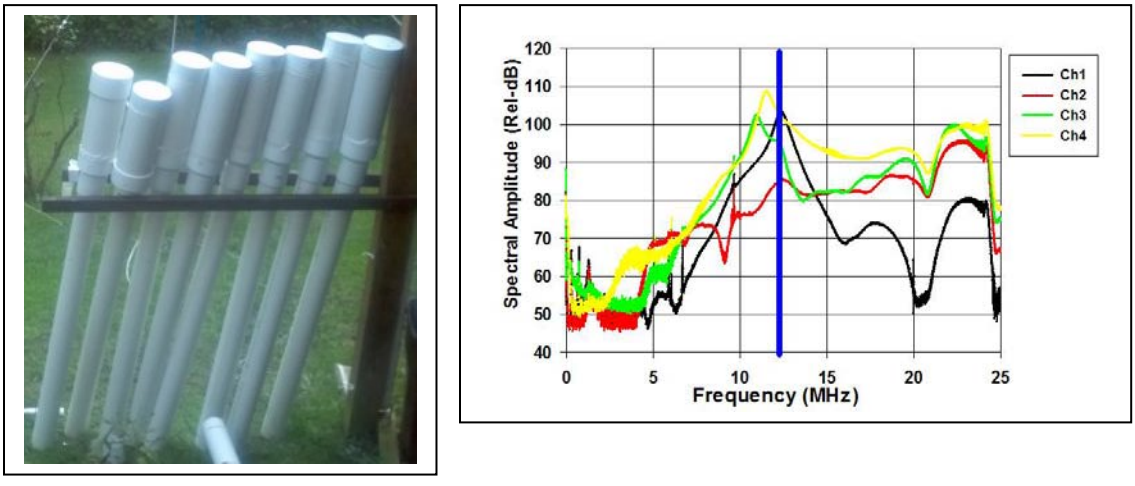

Figure 1. Eight new miniaturized loop antennas at left, with four gain responses shown at right. The first plot in black has been tuned to resonance using a trimming capacitor, while two with lower frequency peaks have not yet been tuned. The plot in red was found to have a cold solder joint, and later repaired.

These elements do not have the bandwidth of our standard 1-m copper pipe loops, but have roughly the same gain at the tuned maximum. The smaller profile and greater weather protection make them better suited for coastal deployments. The 6-inch cylinder enclosure is 18-in high, set upon a 40 - 60-inch tall 4-inch PVC pipe. Loop antennas do not require a good ground screen and are isolated from the ground the higher up they are.

b. *Final integration and testing of the ISR fully digital compact HF radar*
The radar does not contain racks of traditional receiver radio frequency components, but is fully digital in nature, leading to simplified and lest costly construction. A more complicated bistatic version of this radar was built earlier under contract for the Navy, for application to 3-30 MHz simultaneous radar cross section measurements. The radar developed under this NOPP program has been simplified from the Navy version. It consists of five components [a] a receive array of 8-16 elements (as described above), [b] an 8-channel signal conditioning box, [c] a transmit antenna, [d] a power amplifier, and [e] an acquisition computer containing the heart of the HF radar, a fully digital radar transceiver PCI card. Due to it's 10-20% duty cycle, the transmit antenna can be deployed within the receive array, in contrast to FMCW radars of WERA or University of Hawaii design. The radar typically collects 32,768 2-byte samples at 50 MHz sample rate in range delay and 4-Hz repetition frequency, then in real time does pulse compression and digital filtering. This real time processing produces data files of 4-Hz 128 in-phase and quadrature samples that serve as range bin samples identical to the output of a traditional HF radar using traditional RF receiver components. Doppler processing of these samples is done to generate Doppler spectra for current mapping and inversion to directional ocean wave spectra. This digital design reduces the complexity and cost of the HF radar system, projected to be of the order of $50K, including acquisition software, and processing code to invert the Doppler spectra to directional wave spectra. Examples of radar output are shown below.

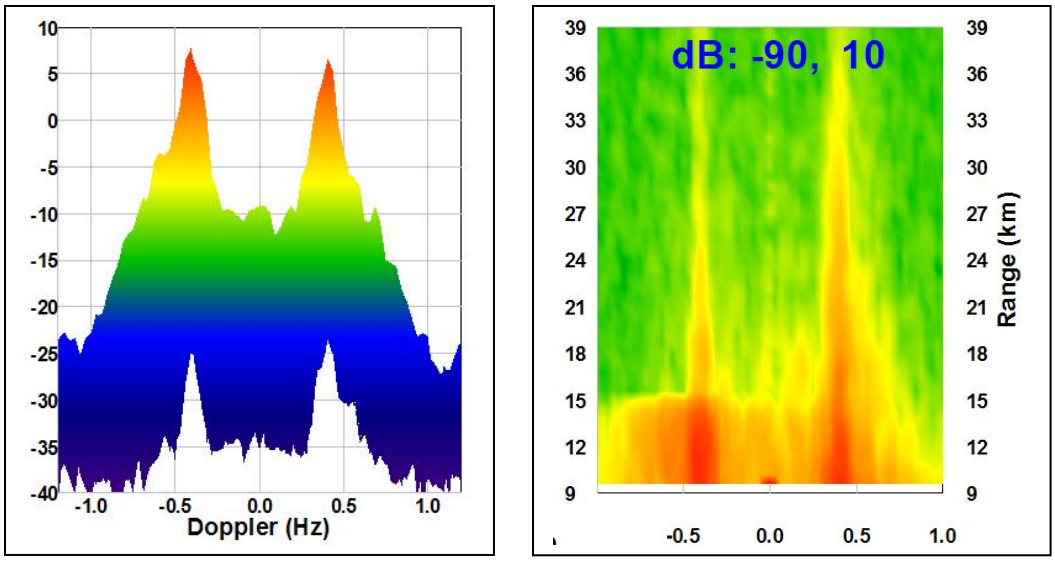

Figure 2a, b. Doppler Spectrum from October storm, Doppler-range spectra same, showing 40 km coverage using 6-watt average transmit power.

c. *Directional Ocean Wave Spectrum Forward Modeling for Spectrum Retrieval.* Software has been generated to forward model the theoretical Doppler spectrum for second order scatter from ocean waves at HF. The Pierson-Moskowitz spectrum is used as input to the scattering model, with wind speed as the input parameter and a fetch dependent amplitude scaling factor. A variety of spreading functions are available, the simplest of which is a small constant plus a COS(2ϕ) spreading function. Results for the forward model are shown below for four different wind speeds, 4, 8, 10 and 12 m/s, and a good fit is obtained using the 8-m/s speed. This model will be cast into backward or retrieval model to determine at a minimum the primary wave direction, RMS wave height, and swell direction and spectral magnitude. A working version of the inversion code should be completed to support the field trials of the two radars in the Spring of 2012.

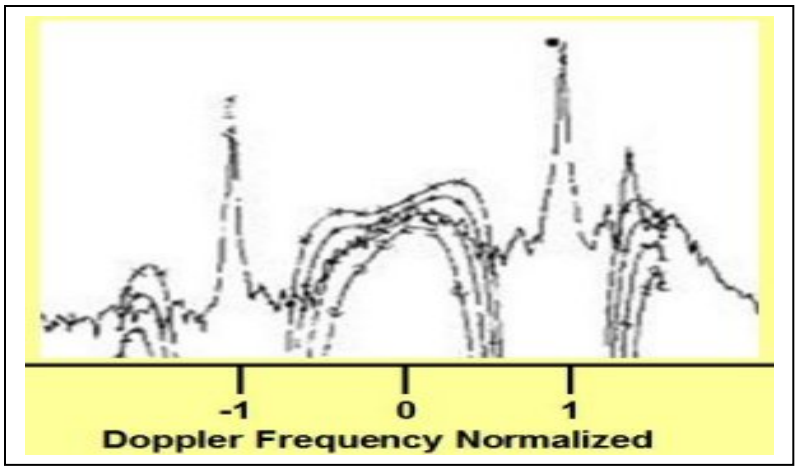

Figure 3. Forward scattering model of the 2nd order Doppler spectrum at HF, to be used as the basis of the inversion code to retrieve directional ocean wave spectra from such HF radar Doppler spectra.

University of Hawaii: Due to buy-out of Innovative Integration by Interconnect Systems Inc., delivery of A/D and CPU subsystem has been delayed in excess of 10 months. Delivery was promised on 8/15. However nearing that date, the company announced that manufactured boards were defective, and that another 9 weeks were need to produce a new batch. At that time, we found through a search that the VP of the company had left to found a new company, Since he was the author of the design of the A/D boards, we decided that it was unsafe to continue working with this company, which appeared increasingly unreliable despite a very complete offering, and cancelled the $155,000 purchase order with legal support from the University.

We secured a second source, D-Tack from Glasgow in Scotland, who had a similar product integrating 32 channel (expandable to 64) and an ARM processor on the same board. They immediately delivered an evaluation board which we were able to use. We put a $180,000 purchase order to this company on September 29. Quantity delivery of 22 boards at $18,000 each has been promised by end of November. All the other components of the radars are completed.

Task 3. High resolution, spatial imaging of wind, waves, currents, and bathymetry. This task involved both ISR and University of Washington. Both have completed their objectives and have published articles providing detailed results (See attachement 2).

The University of Washington completed a study of winds and currents using 2008 data collected on the R/V Thompson. The analysis confirms that a standard marine radar and a custom-built coherent radar, both operating at X-band or 10 GHz, will accurately measure these two quantities. Progress has been made on the measurement of significant wave heights, directional wave spectra, and spatial maps of phase-resolved waves in a circle with a 1.2 km radius around the radar. Significant wave heights obtained from radar cross sections and from Doppler shifts now agree with each other and with buoys very well. Directional wave spectra are in reasonable agreement with those measured on buoys deployed from the ship. Phase-resolved waves from cross sections and from Doppler shifts are highly correlated, although the agreement between them is not perfect.

The two papers "Wave Shadowing and Modulation of Microwave Backscatter from the Ocean" and "Origins of Features in Wavenumber-Frequency Spectra of Space-Time Images of the Ocean" have both been accepted by the Journal of Geophysical Research. The latter paper has been published and the former will soon be published. Both papers acknowledge BOEM support during the research. A third paper showing that whitecaps in deep water are caused by the interference patterns formed on the surface by dominant wind waves was also submitted. It showed that the downwind speed of these patterns matches the breaker speeds that have been measured with video, radar, and acoustics and that these speeds are much smaller than those of dominant waves. The paper got good reviews. Hopefully it will be accepted soon.

Winds and currents from the radar agree within expected tolerances with those measured simultaneously by alternate means – anemometer and a Pitot tube– deployed on the ship. The statistics of waves around a ship or tower - significant wave height, omnidirectional spectra, and directional spectra – also agree well with the more traditional buoy measurements. However, the measurement of the exact locations and heights of "bumps on the ocean" at a particular time still cannot be done sufficiently accurately to be highly useful. Shadowing is insignificant on the open ocean. The low-frequency signal seen in wave number-frequency spectra of radar return is caused by breaking waves located at the points of large slope of the wind-wave interference pattern. The breaking waves are not the dominant waves but waves in the wavelength range 1 to 12 m. The downwind interference pattern moves at a speed well below the dominant wave group speed for wave spectra typical of the open ocean. For more peaked spectra, such as those that might be seen near shore, on lakes, or in wind wave tanks, the speed of the downwind interference pattern is closer to the dominant wave group speed. This means that the wavelength of the breaking waves may approach those of the dominant wave if the spectrum is highly peaked.

The theoretical literature describing the backscatter of HF waves from the sea surface has been reviewed. This work is in support of using HF radar to estimate ocean wave spectra. To second order the coupling has a hydrodynamic and an electrodynamic (EM) part, and these two contributions add separately. Having an accurate expression for these interactions to second order is necessary in order to have an accurate forward model for use in an inversion. However, it has recently been shown that the perturbation expression used for the hydrodynamic modulation of the Bragg scatterers is in error for the effect of gravity waves much shorter than the dominant waves (i.e. those at the peak of the spectrum). A corrected expression is now available in the literature and needs to be incorporated in the inversion. It is not clear whether the EM coupling has an analogous problem, but this question needs to be resolved.

ISR: A coherent rotating marine radar has been developed by ISR for imaging ocean wave orbital wave velocity wave patterns. A patent application, submitted prior to the NOPP onset, was granted to ISR in November of 2012, USPTO #8,305,257: Method and apparatus for coherent marine radar measurements of properties of ocean waves and currents. Elements of the patent are used in the work carried on within the NOPP project.

This NOPP program, Roadmap: Technologies for Cost Effective, Spatial Resource Assessments for Offshore Renewable Energy, has helped finance recent ISR studies. This new coherent radar provides a direct measurement of ocean wave orbital wave velocity, and wave height profiles, without relying on a modulation transfer function (MTF) that has been used with previous systems that map radar echo intensity. The latter approach is prone to error due to environmental dependencies of the MTF, particularly when winds blow into incoming waves, which then produces an enhanced echo strength that is misinterpreted by the MTF scaling as due to larger wave slopes and heights. With this new direct measurement of orbital wave velocity, directional ocean wave spectra can be measured unambiguously, and deterministic ocean wave height fields that can be mapped for real-time input into wave forecasts for platform and ship motion response prediction in real time. A retrieved wave field height map is shown in Fig. 4 below, with pressure sensor locations shown as red crosses. A time series of comparison of individual pixel wave height values is plotted on the right for a pair of pressure sensor locations, as well as the pressure sensor height readings, and the comparison is excellent.

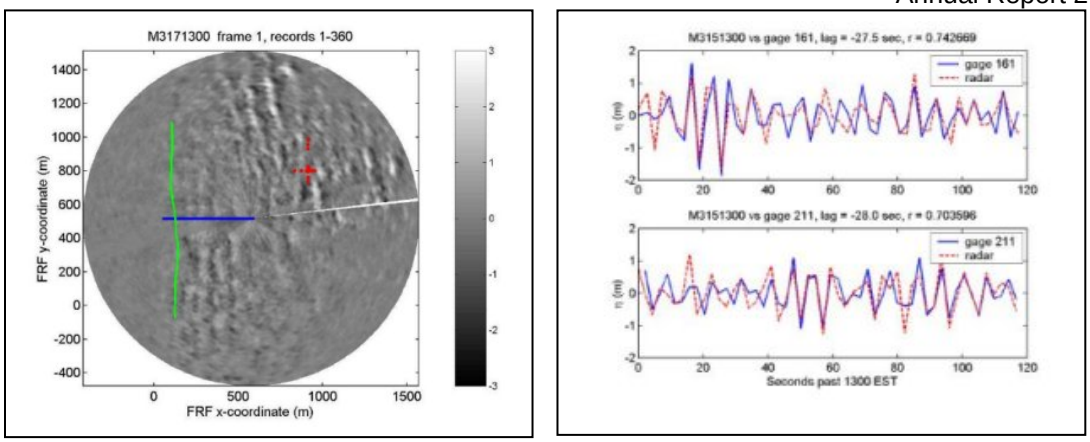

Figure 4. Wave profile image is shown at left, pressure sensors shown as red crosses using the ISR coherent radar. Using many radar rotations, the time series of wave height values from radar pixel locations over two pressure sensors (red) are plotted over height retrieved from pressure sensor array (black), and comparison is quite good.

Given a time series of such wave height maps, one can place a square nest of pixels 64 on a side at any location within the image, and use 3D-FFT processing of the data cube to derive wave height directional spectra. Early tests using standard horizontally polarized antennas produced anomalous results for rms wave height above 3 m, so tests were done using a vertically polarized antenna, with the hypothesis that the outliers were due to wave breaking in deep water that occurred for the higher sea states. Results of tests conducted at the USACE pier in Duck, NC, during the passage of Hurricane Irene are presented below, showing the improvement using vertically polarized antennas, minimizing wave breaking effects for wave heights above 3 m. Comparisons with horizontal polarization for another storm show this dramatic improvement.

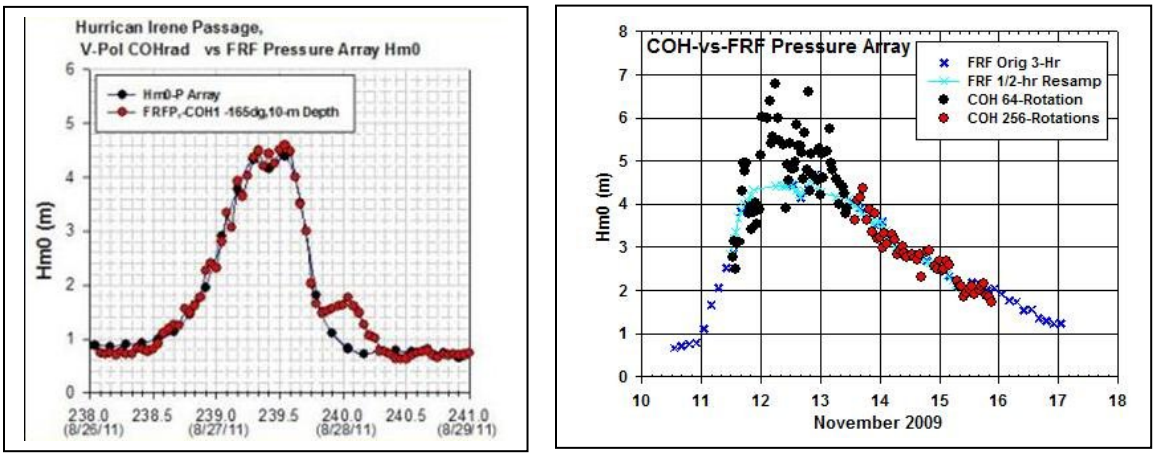

Figure 5. Time series of rms wave height from radar and pressure sensor from two trials show improvement using vertically polarized antenna (l) vs. horizontal (r).

The above wave height maps were created using off-line post-processing software. ISR is developing a new acquisition card that will do the pulse-pair Doppler processing using the FPGA on the card. It will put out in real time range-azimuth slices of wave height profile that can be used for ingestion into real time wave propagation prediction models to predict individual wave crest height that will impact the deep water platform or ship.

Surface currents derived from summing 512 images to produce mean surface currents in an ringed area 400-500 from the radar are shown below for several days of operation.

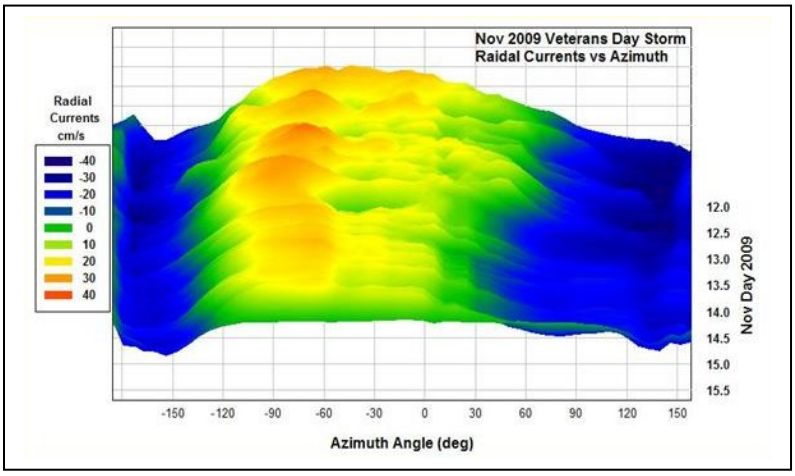

Figure 6. Mean current over 330 deg in azimuth derived from coherent radar data.
In addition to the patent publication, several conference publications were published during the NOPP program, and copies are attached. A journal article is under preparation describing the full capability of the fully coherent marine radar discussed here.

Task 4. Mapping of currents and waves using Doppler sonar.
TRDI ADCPs traditionally vertically project four beams in orthogonal pairs (see the various depiction deployed instruments in Figure 1), and measure the component of the fluid velocity along each beam which allows measurement of several parameters of critical interest in siting and monitoring of renewable energy devices. First, assuming the mean velocity is homogeneous over the horizontal span of the beams (generally a good assumption in the mean), the current can be recovered by differencing opposing beams. Second, since the second order statistics of the wave field are also horizontally homogeneous, the frequency-direction spectrum of the waves can be recovered by a bottom-mounted, upward-looking ADCP in moderate water depths (typically less than 20 m). And third, a great deal of work has been accomplished from ADCPs

Illustration of vertically and horizontally oriented ADCPs

with four and five beams to measure turbulence parameters such as Reynolds stresses and Turbulent Kinetic Energy. That is, a single ADCP can be used to gather measurements of currents, waves and turbulence parameters: three parameters that are of critical interest in site selection and monitoring for renewable energy devices.

Of particular interest to the renewable energy community is the potential to forecast the waves a few seconds into the future. This is because the energy in a typical wave field can rapidly change over several orders of magnitude, and it would be useful to have some short term indicator of a pending large event to allow energy shunting to protect the devices from large events. For turbulence the outer scale turbulence seems far more important than the inertial scale, however there seems to be considerable uncertainty as to what turbulent parameters will eventually prove to have the most utility. Therefore the results from short term wave forecasting are the primary focus of the study.

Acoustic Doppler Current Profilers (ADCPs) can be used to measure wave height and direction, in addition to vertically-profiling currents, and analysis software available from Teledyne-RDI for this purpose that treats the velocity measurements from the various beams and range cells as a sparse array. However, many users make a long wavelength approximation and use conventional triplet processing to estimate wave height and direction from the two horizontal velocity components and a scalar, such as wave height, pressure, or vertical velocity. In fact, because of patent issues, the analysis package provided by Nortek for their AWAC wave-measurement system takes this approach. It is also required if the system is mounted on a moving buoy, ship or Autonomous Underwater Vehicle (AUV) because of the wave-correlated motion of the instrument.

Approximating the horizontal wave velocity by differencing velocity measurements along different (typically opposing) beams is subject to discretization errors that are of order $(k\Delta)^n$, where k is the wavenumber of the wave component being estimated, Δ is the separation of the range cells being differenced, and n denotes the order of the differencing scheme. It has been usual to take n = 1 (i.e. a linear approximation), which has the greatest error for fixed values of k and Δ. We have derived formulas that permit higher order estimation and therefore reduce the bias. They also give improved directional resolution to be obtained in the estimated frequency-direction spectrum.

Wave measurements while underway have to deal with the Doppler shifting of the wave components. This has the effect of mapping intrinsic into apparent (i.e. observed) frequencies. The mapping depends on the direction of the wave component at each frequency. What is less appreciated is that the directional coefficients, when re-mapped to intrinsic frequency (or, equivalently, wavenumber) are biased. We have developed a procedure to correct for this bias.

These ideas are being tested on a data set we recently acquired at the Martha's Vineyard coastal Observatory (MVCO), a facility owned and operated by the Woods Hole Oceanographic Institution, situated slightly south of Martha's Vineyard in 12 m water

depth. The facility includes a bottom-mounted, upward-looking, 1200 kHz Teledyne-RDI ADCP that is cabled to shore. We deployed a Datawell MK-III directional wave buoy close to the ADCP, and flew a REMUS-100 AUV in a box-pattern around the ADCP. The REMUS carries upward- and downward-looking ADCPs, as well as a high-quality Inertial Navigation System (INS). We also equipped it with a Microstrain 3DM-GX3-25 attitude-heading-reference system (AHRS). This is an inexpensive ($1500) inertial sensor. Preliminary estimates of the wave height spectrum and the mean direction at each frequency from the various systems (fixed and moving ADCPs and wave buoy) are shown in the figures below. The AUV was moving approximately upwave at 2 m/s so the Doppler shift and associated biases were not negligible.

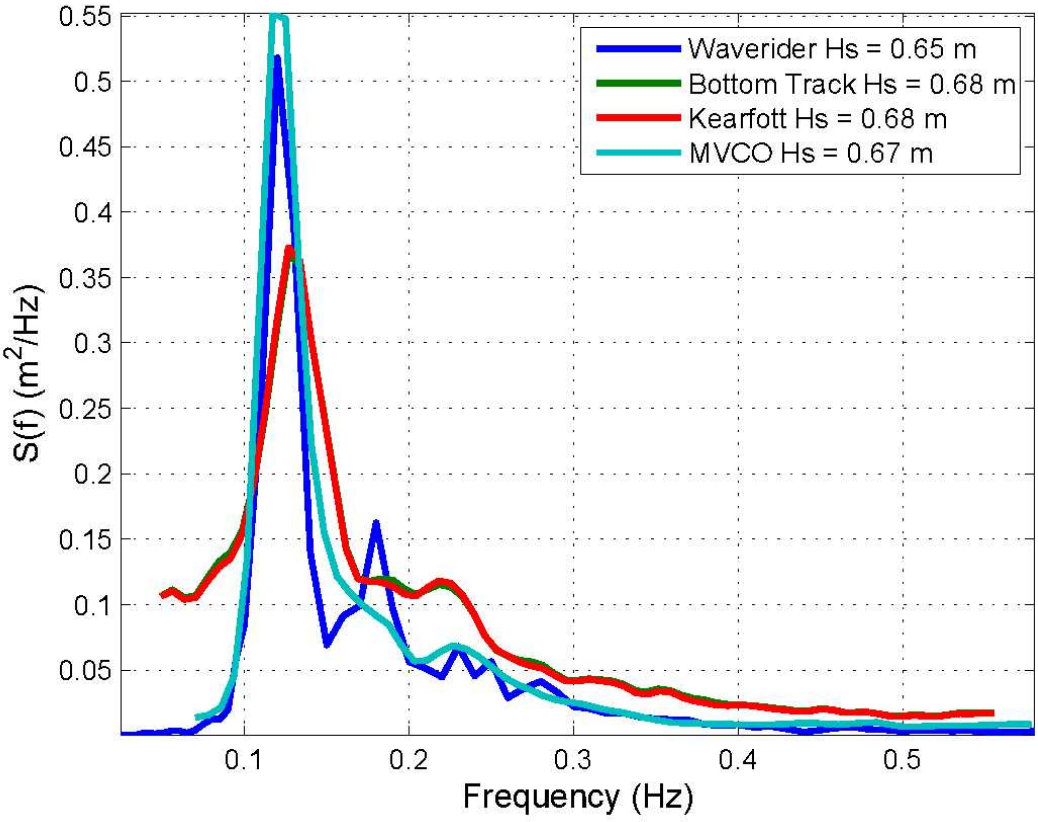

Wave height spectra estimated from a directional waverider (blue), a fixed ADCP (turquoise) and an underway ADCP on a REMUS-100 (red, green)

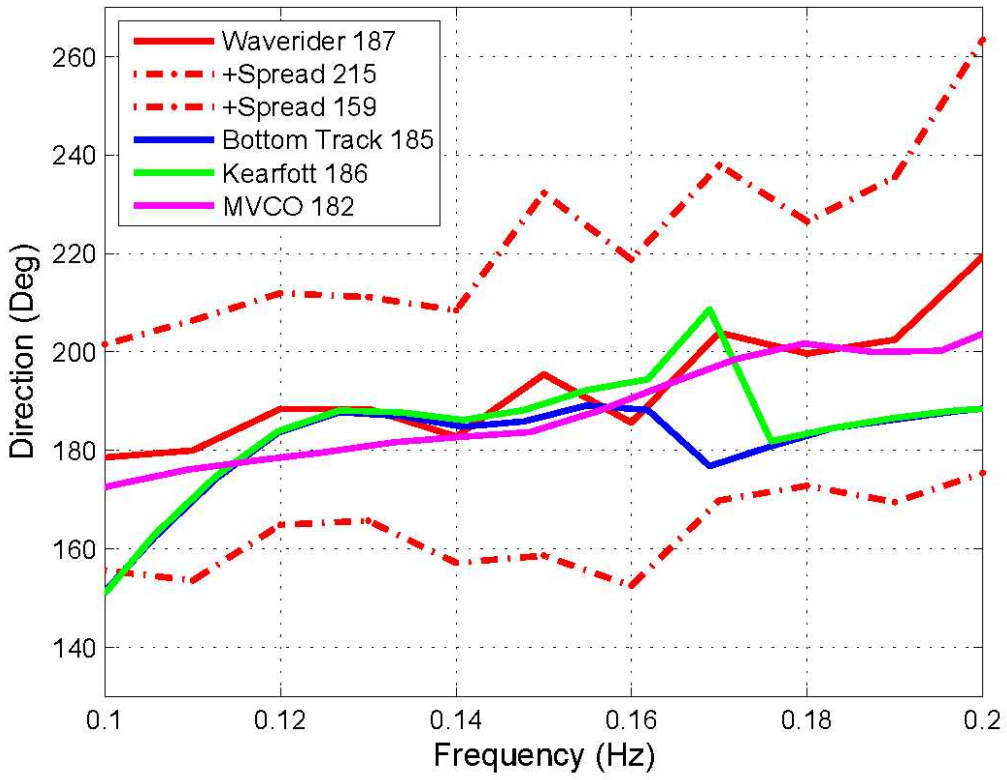

Mean wave direction estimated from a directional waverider (blue), a fixed ADCP (turquoise) and an underway ADCP on a REMUS-100 (red, green)

Task 5. Surveys of sub-bottom, bottom sediment, benthic biotic communities using AUVs.

Shipboard video surveys of sediment features including amphipod mats, redox discontinuities associated with bioturbation, burrows, worm tubes, pseudo feces, and bed forms were completed. Additional sediment samples for infauna validation were collected and analyzed for use with sediment facies identification based on backscatter intensity.

AUV surveys begun for comparison to validated traditional techniques as above. As improvements in AUV modules have become available (ie Klein side scan) repeats of previous surveys have been performed as additional surveys continue with base line data collected earlier. As necessary baseline data has been replicated to reflect slight changes in the environment. Nearly all efforts have been focused upon AUV data collection as availability of the platforms has become predictable.

Baseline data collection using shipboard video cameras documenting fresh water mussel distribution for later use in validation of AUV based video data collection in same location. Use of color balance software investigated for use in post-processing data in

high chlorophyll areas. Several of these surveys have now been replicated with AUV's and demonstrate efficacy of using AUV's.

Image processing and analysis continues using variants of ImageJ software modules. Automated processing not realized for macro algae, but may be useful for infaunal community estimations.

Attachment 1
Schedule

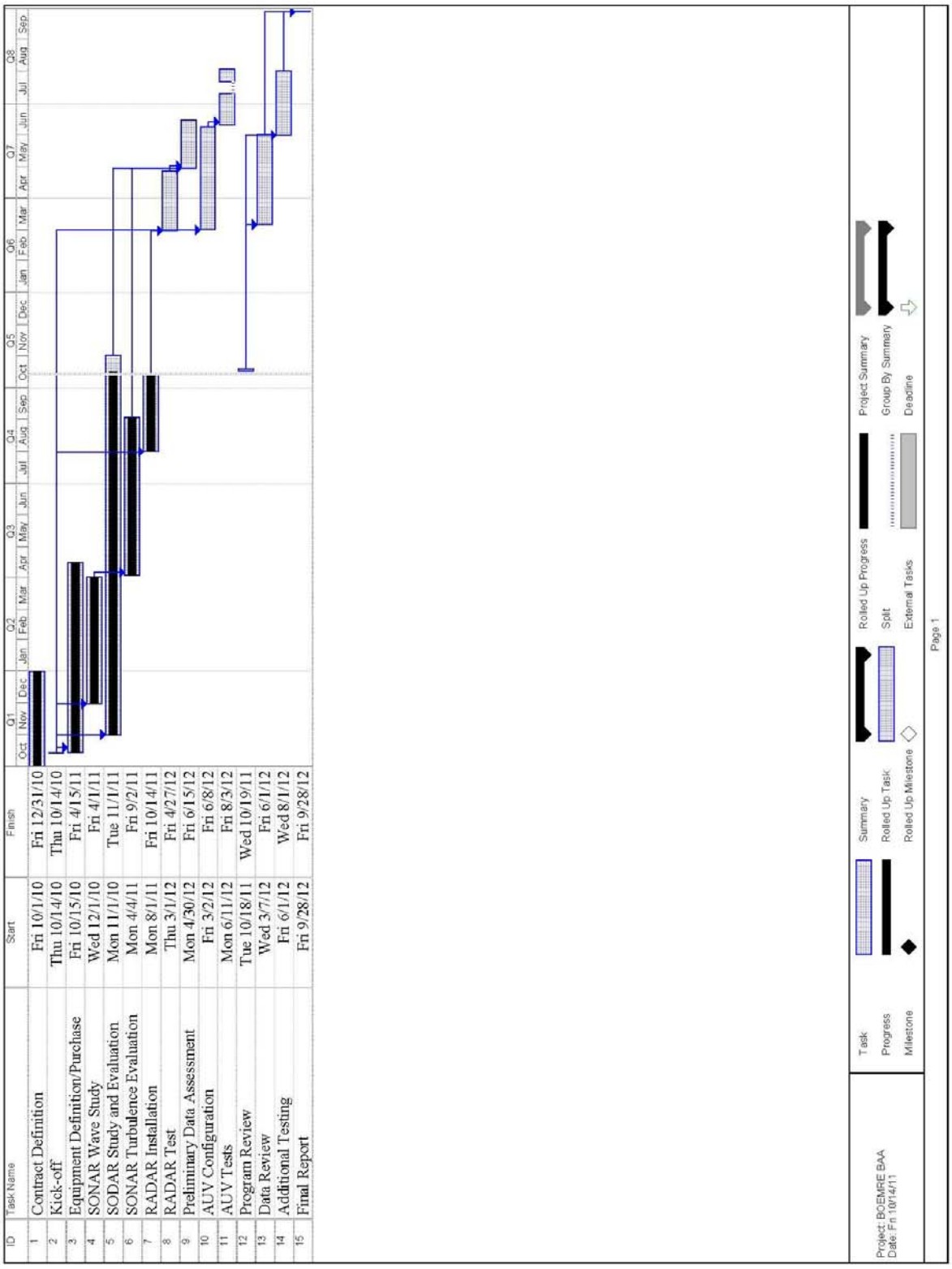

Attachment 2
Articles

Measurement of Winds, Waves, and Currents with a Shipboard Coherent Radar

William J. Plant, Gene Chatham, Kenneth Hayes, and William C. Keller
Applied Physics Laboratory, University of Washington
Seattle WA 98105 USA
plant@apl.washington.edu

Abstract:

In August 2008, we deployed a VV-polarized, X-band (9.36 GHz), coherent radar on a UNOLS ship, the R/V Thompson, on a cruise along the west coast of the United States. The purpose of the cruise was to measure phase-resolved waves around the ship using the low-grazing angle sea return to the radar. The radar signal also proved capable of determining winds and currents around the ship. Here we report these measurements of winds, waves, and currents, and compare them with similar quantities measured by more standard techniques. Wind speeds were determined from wind speed dependence of the upwind maximum of the mean normalized radar cross section (NRCS) measured by the radar. These wind speeds compared well with those measured by the shipboard anemometer. The 180^{o} ambiguity of the wind direction from the radar (because upwind and downwind maxima were nearly the same) was overcome by looking at the direction of propagation of wind waves determined from the wave dispersion relation. This dispersion relation was derived from wave number-frequency spectra obtained from space-time images of both the NRCS and the Doppler offsets. Fitting the dispersion relation to the standard form including currents allowed the current magnitude and direction to be determined. The component of current in the direction of the ship heading agreed well with currents from the ship's pitot tube. Finally, phase-resolved wave fields around the ship were determined using wave-induced variations in the NRCS and Doppler offsets under the assumptions that our k-space azimuthal resolution was high and that NRCS variations were mostly due to changes in local grazing angle, ie, tilt modulation. These phase-resolved wave heights compared fairly well with those measured by a buoy. Significant wave heights and mean omnidirectional spectra also agreed reasonably well with the buoy measurements. However, a close look at the spectra revealed that additional modulation transfer functions were probably necessary to produce accurate wave fields from NRCS variations.

Introduction

Output from microwave marine radars is increasingly being recorded and used to monitor sea-surface features around ships and platforms and to study air-sea interactions (Dankert, et al., 2002; Nieto Borge, et al., 2004, Chang, et al., 2008). The simplest way to produce such data is to tap into the standard marine radar that is available on every ship to record and process the data. This method has proven to be rather effective at producing information about the air-sea interface but it has a number of drawbacks related to the nature of standard marine radars. In particular, these radars are nearly always noncoherent, horizontally polarized on both transmit

and receive (HH polarization), and utilize antennas with very narrow beam widths in the horizontal but very broad beam widths in the vertical. The very narrow horizontal beam width has the large advantage of being able to produce images of waves travelling in all directions, although it is sometimes forgotten that waves travelling perpendicular to the antenna look direction are severely reduced in amplitude.

Being noncoherent, the standard marine radar produces only half the information available in received fields. The magnetron used in these radars does not maintain its phase from pulse to pulse and therefore, without modification of the radar, the phase information in the received signal is lost. The modulation of the received power is available to obtain wind, wave, and current information but the Doppler part of the signal is not. Furthermore, HH polarization was originally chosen for these radars not only because such waveguide antennas are easier to produce than VV polarized antennas but also because it suppresses the sea return outside of regions of breaking waves. When the goal is the detection of objects on the surface, such suppression of sea return (noise) is very useful. The difficulty becomes distinguishing target return from breaking wave return rather than locating targets within a field of backscatter of similar magnitude over the whole sea surface.

When the goal is to utilize the sea return as the signal, the low level of HH polarized return away from breaking waves becomes a drawback, causing parts of the surface to appear to be shadowed due to their low return (Plant and Farquharson, 2012). Furthermore the broad vertical beam width of the antenna causes nearly half of the transmitted power to be directed upward, away from the sea surface. The part of the transmitted signal that does strike the sea surface, when combined with the R^{-3} fall-off of the received power, where R is range, causes most of the sea return to come from the region near the ship. Consequently, even when transmitting 25 kW of power, marine radars typically observe sea return only out to 2 km or so. Finally, the very broad vertical beam width of these antennas makes it very difficult to calibrate a standard marine radar to obtain the normalized radar cross section of the sea (NRCS) from the received power.

In an attempt to overcome these drawbacks of marine radars, we have deployed a VV-polarized, X-band (9.36 GHz), coherent radar with four pencil-beam antennas on a UNOLS ship, the R/V Thompson, on a cruise along the west coast of the United States in August 2008. This radar, which we call CORAR for COherent Real Aperture Radar, was designed and constructed at the Applied Physics Laboratory of the University of Washington (APL/UW). Here we report measurements of winds, waves, and currents using CORAR and their comparisons with more standard measurement techniques.

The Coherent Real Aperture Radar (CORAR)

In addition to collecting the received power available from standard marine radars, CORAR maintains the phase of the return signal in order to produce complete Doppler spectra at each range bin. The first three moments of these spectra are computed and stored in real time, along with a subset of the complete spectra. These moments correspond to the received power (zeroth moment), the Doppler offset (first moment) and the Doppler bandwidth (second moment). They were stored at each of 256 range bins in each of 64 different azimuthal directions. Due to storage limitations, complete Doppler spectra were stored only for every 16^{th} range bin. The

radar was calibrated on an outdoor antenna range at our laboratory so that received power could be converted to calibrated NRCS values in subsequent processing. Also in subsequent processing, Doppler offsets were converted to horizontal Doppler velocities simply by adjusting for signal-to-noise ratio, multiplying by one-half of the microwave length and dividing by the cosine of the grazing angle. All of these techniques have been reported in detail for similar radars (Plant et al., 1998).

CORAR transmitted only 40 watts of peak power but coherently averaged 16 pulses to increase the signal-to-noise ratio. Furthermore, the radar utilized two-foot parabolic antennas to increase the antenna gain compared to a standard waveguide antenna, thus concentrating more power on the sea surface. The result was a maximum range of 1 to 2 km, depending on wind speed, quite similar to standard marine radars transmitting much higher power. Because we calculated that the minimum time necessary to obtain Doppler spectra with sufficiently high frequency resolution and signal-to-noise ratio was 41 msec, the antenna rotation rate had to be much slower than that of a standard marine radar; rather than 1 to 2 sec, it was 13.2 sec. In order to make the revisit time of any azimuth angle approach that of a marine radar, we deployed four rotating antennas looking 90^o apart on a stabilized mount. Figure 1shows CORAR deployed on the R/V Thompson. The returns from these four antennas were interleaved in the final processing so that the output closely resembled the output of a single antenna rotating at 13.2/4 = 3.3 sec. Dealiasing of wavenumber-frequency spectra, as discussed in more detail below, further increased the effective temporal resolution by a factor of three, to about 1.1 sec between looks. Specifications of CORAR are given in Table 1.

Figure 1. The APL/UW coherent real-aperture radar CORAR mounted on the R/V Thompson. All four parabolic antennas are vertically polarized.

The antenna mount used on the ship was able to stabilize the antennas only to within rms angles of about 1^o. Thus it was necessary to determine the precise grazing angle of each antenna in order to convert received power to NRCS. This was accomplished by smoothing the return

power along each look direction and determining the range of the maximum power return. From this maximum, the boresight grazing angle of the antenna could be determined using the radar equation, the parameters of the radar, and an approximate dependence of NRCS on grazing angle. The inferred boresight angles from the four antennas tracked each other very well. The NRCS values used to determine wind speed and direction below were averaged over a range of grazing angles from 1^o to 3^o (Plant et al., 2010).

We averaged over the same range of grazing angles to produce mean Doppler velocities in each look direction before detrending. The ship speed and Bragg wave phase speeds were removed from these mean Doppler velocities and they were compared with currents inferred from the first-order dispersion relation observed in wavenumber-frequency spectra of time series of range returns in each look direction. This will be discussed in more detail later.

To measure the wave height, it was necessary to detrend both the NRCS and the measured Doppler velocities to get their deviations from the local mean values. Because of the broad (3.5^o one-way) horizontal beam widths and the filtering around the dispersion relation that we used to eliminate noise (see below), variations in NRCS and Doppler velocities were caused by surface waves travelling very nearly in the antenna look direction. Thus we related them to the component of local surface wave slope and orbital velocity in that direction. Note that this assumption will become less good for longer waves. The horizontal components of measured line-of-sight Doppler velocities were used in order to maintain the phase of the orbital velocities of these waves across ranges. Detrending the NRCS was necessary due to its natural decrease with decreasing grazing angle. The reason to detrend measured velocities after conversion to horizontal values was primarily to remove ship motions. Mean values of both ship velocity and currents are horizontal so that they should not vary with range. However, variations of the ship motion, that is variations in boresight caused by pitch and roll, always produce radial velocities that yield constant Doppler shifts with range and therefore larger horizontal Doppler velocities at small ranges. We detrended the spatial variations of both NRCS and Doppler velocities by Fourier transforming, setting the two lowest-wavenumber bins to zero, and inverse transforming. This means that variations longer than 420 m will not be included in our analysis.

The R/V Thompson Cruise

From August 9 to 18, 2008, we mounted CORAR on the R/V Thompson on the roof of the wheel house for a cruise along the west coast of the United States. CORAR mounted on the Thompson is shown in Figure 2a while the track of the cruise is shown in Figure 2b.

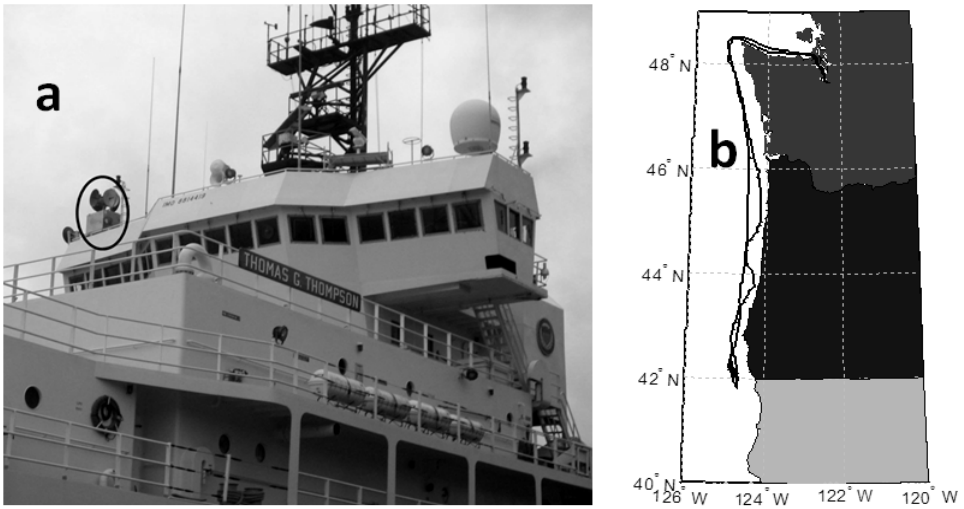

Figure 2. a) The APL/UW coherent radar, CORAR (circled), mounted on the R/V Thompson. b) Ship track on the August 9 to 18, 2008 cruise.

Wind conditions during the cruise are shown in Figure 3. CORAR began collecting data with its antennas rotating on the morning of August 10, while the ship was in transit to its primary station off the Oregon/California border. Except for some intermittent periods of downtime, CORAR continued to operate in this mode until the evening of August 13. At that point we switched to non-rotating modes, first for interferometric studies and then for studies of space-time data. The latter study has already been reported (Plant and Farquharson, 2012) and the interferometric study will not be reported here.

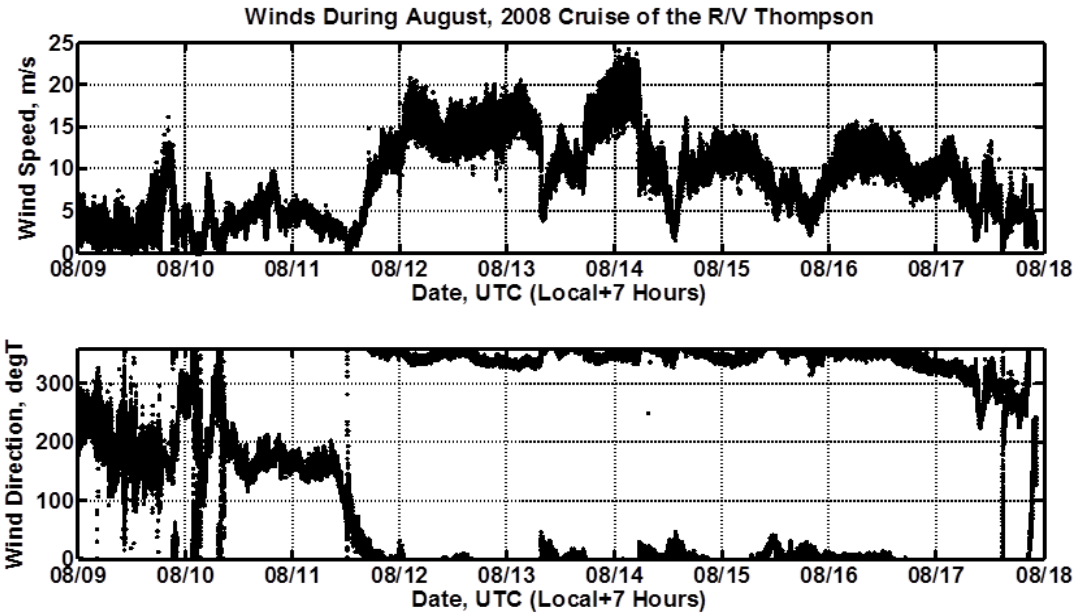

Figure 3. Wind conditions during the remote sensing cruise of 2008 on the R/V Thompson.

During the cruise, the University of Michigan deployed two buoys on August 13. The buoys were tethered to the ship rather than moored due to the depth of the water. Omnidirectional wave height spectra from these buoys will be shown below for the following time periods on August 13: 09:53:07' to 10:27:14, 13:50:25' to 14:24:33', and 17:37:16' to 18:11:25'. Because August 13 will be an important day in the data to be discussed, we show in Figure 4 the ship speed, heading, and track during this day.

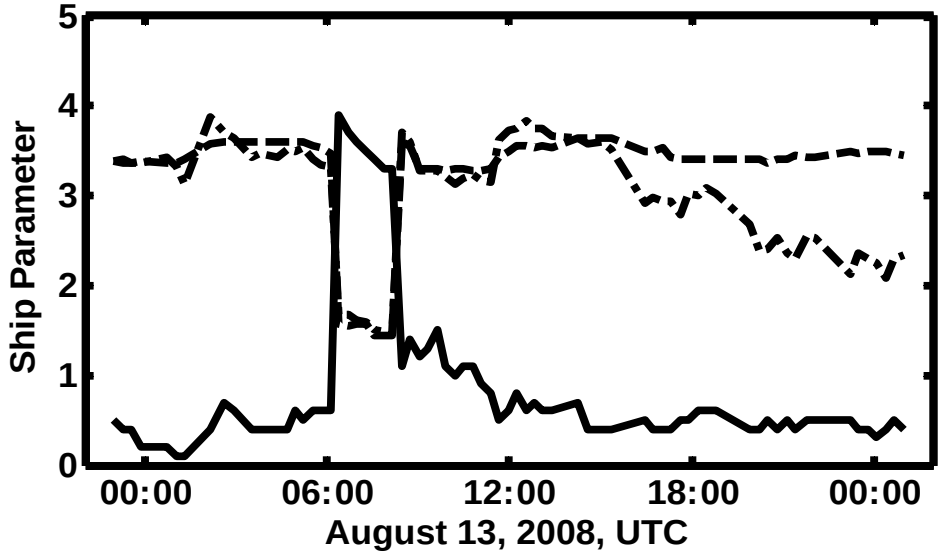

Figure 4. Speed, heading, and track of the R/V Thompson on August 13, 2008. The solid curve shows the ship's speed in m/s, the dashed curve shows its heading in ^{o}T divided by 100, and the dash-dotted curve shows its track in ^{o}T divided by 100.

Wind Measurements

The basis of our radar wind measurements was our observation that at VV polarization the azimuth-angle dependence of the NRCS showed the same second-harmonic behavior that is familiar at both polarizations at lower incidence angles (Plant et al., 2010; Jones et al., 1977). This is not true for the HH polarization used by most marine radars, where a single, broad upwind peak exists to produce a first-harmonic behavior. Figures 4a and 4b show the results from Plant et al. (2010). On most ships, intrastructure blocks part of the field of view. For the broad peak characteristic of HH polarization, this can often make it difficult to detect the upwind peak. For the two narrower peaks characteristic of VV polarization, on the other hand, even severe blockage by superstructure does not obscure both peaks. This is illustrated in Figure 5c where NRCS data from this cruise averaged over the grazing angle range from 1^{o} to 3^{o}. For azimuth angles greater than 200^{o} clockwise from the bow, the superstructure interferes with the sea return. Nevertheless, the second harmonic behavior of the NRCS is clear.

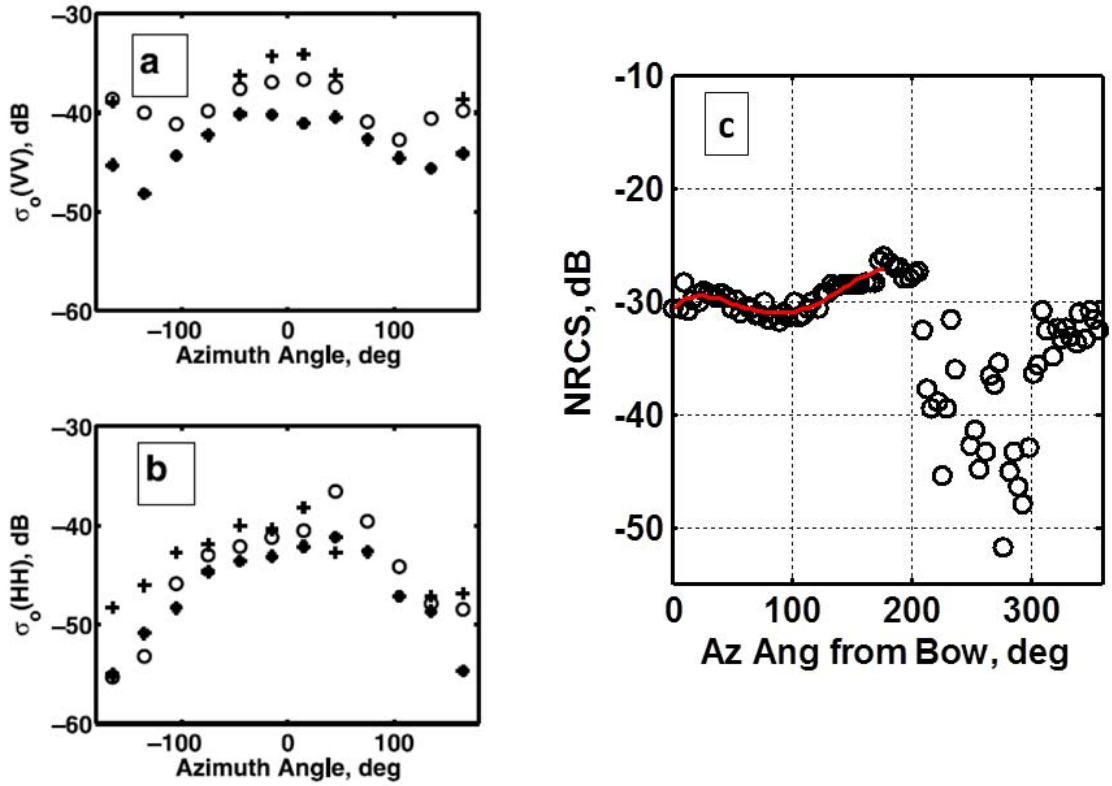

Figure 5. a) Azimuth angle dependence of the VV polarized NRCS for wind speeds of 4, 6, and 8 m/s (from Plant et al., 2010). b) Same as a) but for HH polarization. c) Azimuth angle dependence of the NRCS, averaged between grazing angles of 1^o and 3^o, measured on this cruise at a wind speed of XX m/s. The ship's superstructure interfered with the sea return at angles above 200^o. The red curve is a fit to the data over the angular range 0^o to 200^o.

Using this feature of VV backscatter, we needed only choose the upwind peak and determine the NRCS level there. We derived a model of the expected wind speed dependence of the upwind NRCS using the multiscale model described by Plant (2002). We found that the dependence given by the model was well represented by the following equation:

$$\text{NRCS (upwind)} = -1.05(U-0.9)^2 + 13(U-0.9) - 61.5$$

Figure 6a compares this model (black curve) with data taken on earlier cruises (Plant et al. 2010). Occasionally the downwind maximum of the NRCS was comparable to the upwind one. We were assured of choosing the upwind peak by observing the direction of wind-wave propagation given by the radar-derived dispersion relation, as will be described in detail below. Figure 5b shows the behavior of the log-grazing-angle NRCS at VV polarization and will be used later for wave retrieval.

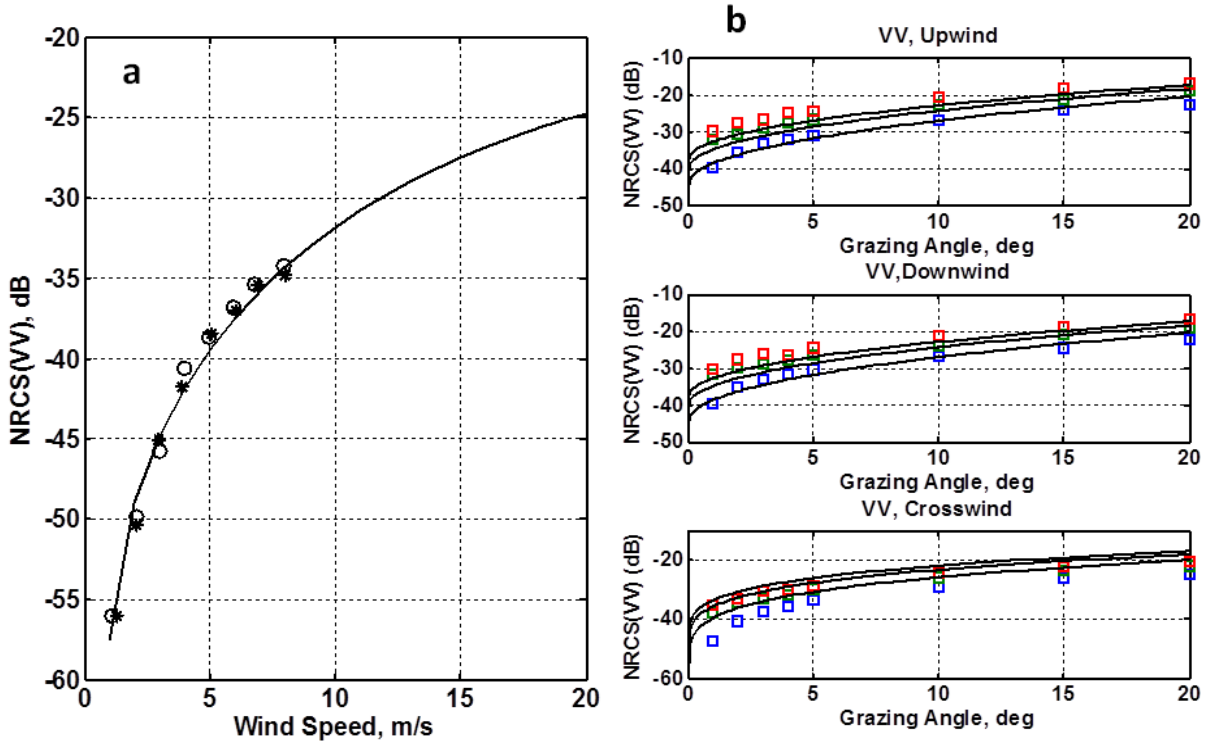

Figure 6. a) The model function used here to retrieve wind speeds (black curve) compared with data taken on two earlier cruises in 2005 (asterisks) and 2006 (circles) [Plant et al., 2010]. Data and model are for upwind looks at grazing angles between 1^o and 3^o. b) Dependence of the normalized radar cross section in dB on grazing angle. Squares show predictions of the multiscale model at wind speeds of 4 (blue), 8 (green), and 12 m/s (red) (Plant, 2002). The curves show $\sigma_o(\theta_g)$ used for wave retrieval at the same wind speeds.

Figure 7 compares wind speed and direction obtained from the radar with those given by the ship's anemometer on August 13. The rms difference between speeds from the ship's anemometer and the radar is 2.8 m/s while that between the directions is 18^o. This is sufficiently encouraging to believe that a VV polarized radar on a ship can yield viable wind fields around the ship, perhaps with somewhat refined antennas and model function.

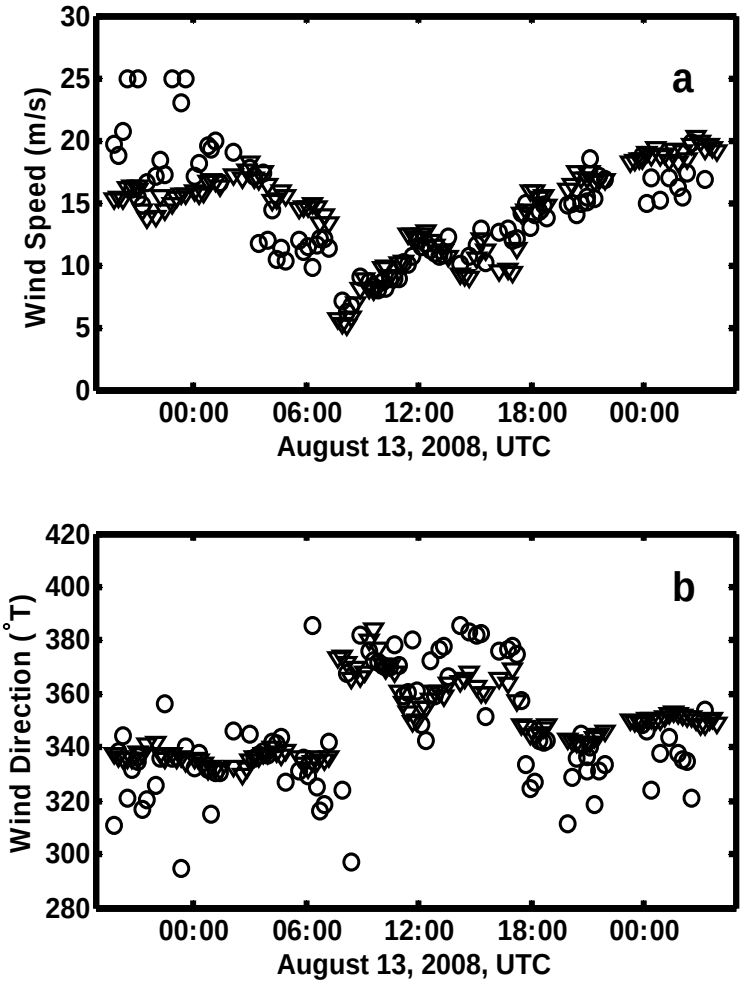

Figure 7. a) Wind speeds from radar (open circles) compared with those from the ship's anemometer (triangles). b) Wind directions from radar (open circles) compared with those from the ship's anemometer (triangles). Rms differences in speed and direction are 2.8 m/s and 18°, respectively.

Current and Doppler Measurements

As our antennas rotated, we obtained the spatial dependence of both the cross section and scatterer velocity every three seconds in any particular direction. Two-dimensional spectra of such space-time series are displayed in Figures 8a and 8b while the antenna was looking into the wind. The dashed lines in these plots show the first-order dispersion relation

$$\omega = \sqrt{gk} + \mathbf{k} \cdot \mathbf{U}$$

where ω is angular frequency, **k** is wave vector and k is its magnitude, g is gravitational acceleration and **U** is the current vector. In Figure 8, we have set U to be the negative of the

component of ship velocity along the antenna-look direction. The dispersion relation folds back at the upper and lower Nyquist frequencies of 0.15 Hz. (Note that this is the Nyquist frequency for NRCS and Doppler velocity samples, not for the Doppler spectrum.) Wave energy clearly lies near the first-order dispersion relation but it is aliased due to our 3.3 sec revisit time. Other features that lie off the first-order dispersion relation can also be seen in the spectra. These higher-order features have been identified as being primarily due to breaking waves (Plant and Farquharson, 2012; Plant, 2012).

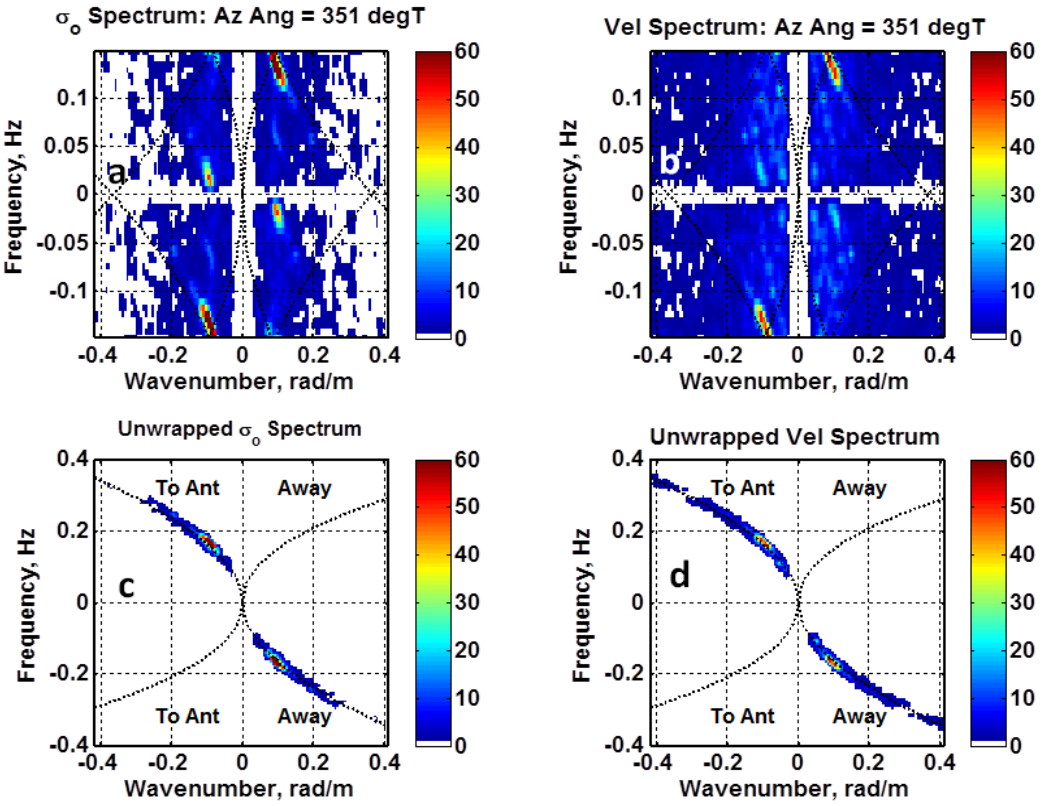

Figure 8. Wavenumber-frequency spectra of space-time images obtained from CORAR when looking into the wind. The top row are original, aliased spectra and the bottom row are dealiased, filtered spectra. The left row is from space-time images of NRCS while the right row is from Doppler velocities. The sampling rate was 3.3 seconds.

We may unwrap these spectra by translating the bottom half to sit on top of the figure and the top half to lie beneath the bottom of the figure. If these unwrapped spectra are filtered with a wide bandwidth around the nominal first-order dispersion relation, ie, one that includes only ship motion, and only the branch with the highest level of energy above is kept, the spectrum clearly indicates the direction of wave travel. This is shown in Figures 8c and 8d. In this case, it is clear that the wind waves propagate toward the radar since the antenna is looking upwind. In some directions, the wave components were very low and neither branch of the dispersion curve clearly contained the most energy. In these cases we were unable to determine a wave direction, or even the existence of waves, and we assumed that no waves existed in this direction.

Assuming that the radar responds only to waves travelling along the direction in which the antenna is looking, the component of current in that direction can be obtained by fitting the dispersion relation to the unwrapped, filtered data taken when waves are clearly evident. We did this by varying the component of U along the antenna-look direction until we obtained the best fit to the maxima of the return power as a function of wavenumber and frequency. If this is done for all look directions and the ship velocity subtracted in each direction, then the current produces a sinusoidal plot versus azimuthal look direction. It is a simple matter to pick the current magnitude and direction.

We had no comparison measurement of current magnitude and direction during our cruise. However, a pitot tube was located near the bow of the ship at a depth of about 3 meters pointing in the direction of the ship's heading. This pitot tube gave a value for the component of current in the heading direction when the ship speed was subtracted. These are compared with current components from the radar in the same direction in Figure 9. The agreement is very good, with an rms difference of . This supports the validity of the radar measurements of current.

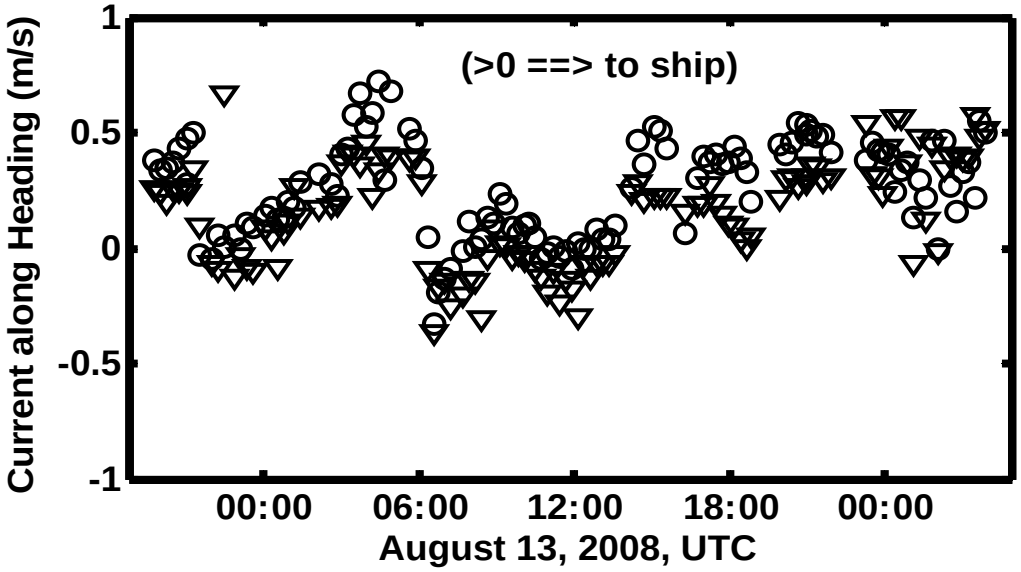

Figure 9. Time plot of the current in the direction of the ship's heading as measured by the ship's pitot tube (triangles) and by the radar (circles). The rms difference between these two time series was .

Since CORAR is coherent, one might think that the centroid (first moment) of mean Doppler spectra could be used to measure currents in addition to the method relying on the dispersion relation described above. However, our measurements emphatically show that the mean Doppler centroid is not primarily a measure of the current. Figure 10 compares the current measured using the dispersion relation with the apparent currents derived from the Doppler centroid. Both measurements were made at 21:00 UTC on August 13. The Doppler centroid yields apparent currents that are much larger than those derived from the dispersion relation. Furthermore, the apparent current obtained when the antenna was looking upwind (upwave) is larger than that obtained when looking downwind. It appears that the correlation between received power and Doppler offset first described by Hasselmann and Schieler (1970) dominates the Doppler

centroid in this case. This correlation is evidently higher looking upwind when breaking waves contribute more to both the received power and Doppler velocity than when looking downwind.

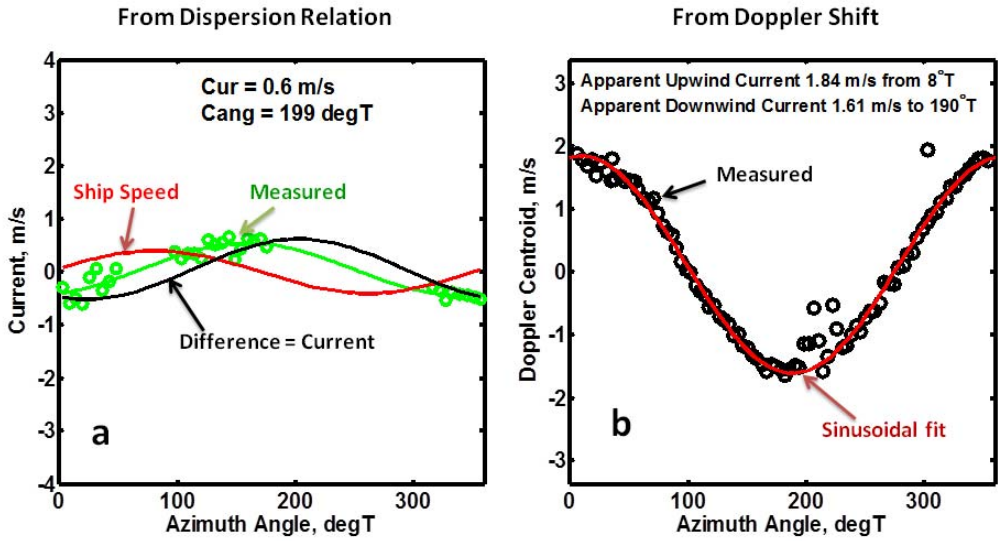

Figure 10. Comparison of currents measured using the dispersion relation (a) with apparent currents from the Doppler centroid (b). Both sets of measurements were obtained on August 13, 2008 at 21:00 UTC. The wind speed was 16.9 m/s from 341°T.

Wave Measurements, Phase-resolved and Statistical

Having determined the wave propagation direction and the current component in cases when waves were clearly evident in a particular antenna-look direction, we then filtered more tightly around a dispersion relation that included the current and ship velocity. We kept both the filtered spectrum and the filtered Fourier transform (whose magnitude-squared is the spectrum) that resulted from these procedures. Thus, we kept the components of the variations of the NRCS and Doppler velocities that resulted from the action of the linear part of the surface waves; nonlinear effects were discarded. Recall that only variations with wavelengths less than 420 m are included in our analysis. Inverse transforming these quantities produced the spatial and temporal variations of the NRCS and Doppler velocities caused by the first-order surface waves.

From these variations in the NRCS and Doppler velocities, one can, in principle, obtain the surface-wave height. For the variations in Doppler velocities, the procedure is straightforward. At each time step, the measured spatial variations in Doppler offset, $f_d(R,t)$, in a given direction, indicated by "i" are converted to velocity:

$$V_i(R,t) = \frac{\lambda_o f_{di}(R,t)}{2\cos\theta_{go}}$$

where R is range, λ_o is the microwave length, and θ_{go} is the mean grazing angle at that range. Then the surface displacement, η_i, is easily obtained in K-space:

$$\eta_1(K,t) = \frac{V_1(K,t)}{\omega_1(K)}$$

The Fourier transform of $\eta_1(K,t)$ is the desired $\eta_1(R,t)$. Because the velocity at the wave crest changes signs when the wave travels the opposite direction, we have to set

$$\eta_1(R,t) = -\mathrm{sgn}(K) * \eta_1(R,t)$$

where sgn(K) is positive for waves traveling in the range direction and negative in the opposite direction. We let sgn(K) = 0 when waves could not be detected in a given direction.

The procedure for transforming temporal-spatial variations in received power into wave amplitude is not so straightforward. We may write the received power, P_r, as follows:

$$P_r = \frac{C\,\sigma_0 A}{R^4} = \langle P_r \rangle + \langle P_r \rangle \left(\frac{\delta P_r}{\langle P_r \rangle} \right) = \langle P_r \rangle + \langle P_r \rangle \int m(K) S(K,t) \exp(-iKR)\, dK$$

where C is constant, σ_o is normalized radar cross section, A is the area of a resolution cell, brackets indicate a spatial average, m is the modulation transfer function, S is (large-scale) surface slope, K is the long wave number. For pulsed radars such as CORAR, A is proportional to $R/\cos\theta_g$. Since σ_o is a function of grazing angle, θ_g, and the small scale roughness spectrum, ψ, we have

$$\frac{\delta P_r}{\langle P_r \rangle} = \frac{\delta \sigma_o}{\langle \sigma_o \rangle} + \frac{\delta \sec\theta_g}{\sec\theta_{go}} - \frac{3\delta R}{\langle R \rangle} = \left(\frac{1}{\langle \sigma_o \rangle} \frac{\delta \sigma_o}{\delta \theta_g}\Big|_{\theta_{go}} + \tan\theta_{go} \right) \delta\theta_g + \frac{1}{\langle \sigma_o \rangle} \frac{\partial \sigma_o}{\partial \psi}\Big|_{\langle\psi\rangle} \delta\psi - \frac{3\delta R}{\langle R \rangle}$$

where θ_{go} is the mean grazing angle at range R. But

$$\delta\theta_g = \frac{d\eta}{dR} = S$$

and

$$\frac{\delta R}{\langle R \rangle} = \frac{\eta}{h}$$

where h is the height of the antenna. Fourier transforming, we may make the following identification:

$$m(K) = m_t + m_h(K) + m_r(K)$$

where the tilt modulation transfer function (MTF) is

$$m_t = \frac{\partial \ln\langle\sigma_o\rangle}{\partial\theta_g}\Big|_{\theta_{go}} + \tan\theta_{go}$$

the hydrodynamic MTF is

$$m_h(K) = \frac{1}{\langle\sigma_o\rangle}\frac{\partial\sigma_o}{\partial\psi}\frac{\delta\psi}{S}\Big|_{\langle\psi\rangle}$$

and the range-change MTF is

$$m_r(K) = \frac{3}{Kh}$$

Then,

$$\frac{\delta P_r}{\langle P_r \rangle} = \int m(K) S(K,t) \exp(-iKR)\, dK$$

This is the standard view of the MTF when received power is not calibrated into NRCS. By Fourier transforming the spatial variations in P_r, dividing by m(K), and inverse transforming, one obtains S(R,t). However, we relate P_r to σ_o using mean values of A and R. This means that

$$\frac{\delta P_r}{\langle P_r \rangle} = \frac{\delta\sigma_o}{\langle\sigma_o\rangle}$$

and the $\tan\theta_{go}$ term is not in m_t and $m_r = 0$. Therefore, we have

$$S(R,t) = \frac{1}{\langle\sigma_o\rangle}\int \frac{\delta\sigma_o(K,t)}{m(K)} \exp(iKR)\, dK$$

The above MTF definitions are valid in deep water when the wave travels toward or away from the antenna. The hydrodynamic MTF, which accounts for long-wave-induced variations in small-scale roughness, is poorly characterized but known to be a function at least of microwave frequency, wind speed, wind direction, and K (Keller and Plant, 1990; Plant et al., 1993; Hara and Plant, 1994). Although its value varied somewhat from one data set to another and depended on the value assumed for the relaxation time, Hara and Plant found that m_h was always less than 12 in magnitude. On a Bragg/composite surface model, the tilt MTF is between 77 and 230 for grazing angles between 1^o and 3^o for a pulsed radar like CORAR. Therefore, we shall follow Dankert and Rosenthal (1994) and omit m_h in

the calculations to follow. We note, however, that this may not be an entirely satisfactory assumption since m_h is in phase with the wave amplitude while m_t is 90° out of phase.

With these assumptions, $m(K) = m_t$ is not a function of K so we have:

$$S_i(R,t) = \frac{1}{m_t(\sigma_o)} \int \delta\sigma_o(K,t) \exp(iKR)\, dK = \frac{\delta\sigma_o^{dB}(R,t)}{m_t^{dB}}$$

where $\delta\sigma_o^{dB}(R,t)$ is the measured cross section in dB that has been detrended, m_t^{dB} is m_t converted to decibels, or $m_t^{dB} = 23\, m_t$.

It is most convenient to implement this equation for S by finding the difference in grazing angle, $\theta_g - \theta_{go}$, where the measured $\delta\sigma_o^{dB}(R,t)$ is equal to $\langle\sigma_o^{dB}(\theta_g)\rangle - \langle\sigma_o^{dB}(\theta_{go})\rangle$ given by a model function. Then $S_i = \tan(\theta_g - \theta_{go})$. Once the slope has been determined, it is straightforward to determine $\eta_i(K,t)$:

$$\eta_i(K,t) = \frac{S_i(K,t)}{jK}$$

where $j = \sqrt{-1}$. $\eta_i(R,t)$ is then the Fourier transform of $\eta_i(K,t)$. No multiplication by sgn(K) is necessary in this case because increased power return always come from the side of the wave facing the antenna. We still set $\eta_i = 0$ in directions where no waves could be detected, however.

In practice the determination of the model function $\langle\sigma_o^{dB}(\theta_{go})\rangle$ was done by attempting to get the best match between waveheights from Doppler shifts and those from the NRCS. The resulting model function, which had to include a dependence on wind speed, was checked against predictions of the multiscale model (Plant, 2002). The results are shown in Figure 6b. Note that only the slope of the resulting model function is required to retrieve wave heights. Figure 11 shows wave heights in different look directions derived from both the NRCS and Doppler velocities. The figure shows, from top to bottom, wave heights looking upwind, downwind, up swell, and down swell. While wave heights measured by the two different methods are certainly not identical, they are well correlated. Because of our spectral unwrapping procedure, such plots can be produced every 1.1 seconds so that one can easily look at many comparisons. The one shown is fairly representative. We will look into the similarities and differences of the results of the two methods in more detail below.

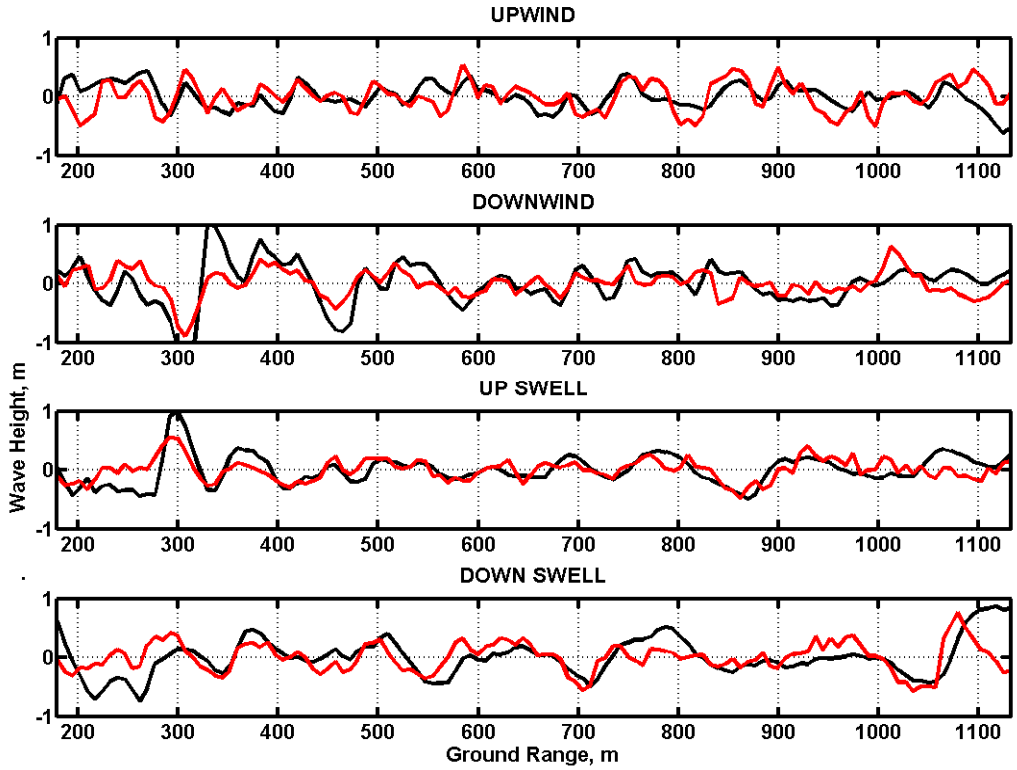

Figure 11. Comparison of wave heights derived from Doppler offsets (red) and received power (black). From the top, the directions of look are upwind, downwind, up swell, and down swell. Data were taken on August 13, 2008 at 17:57 UTC

We used these measurements along the various azimuth angles to determine the two-dimensional, phase-resolved surface displacements around the ship. The results obtained above for $\eta_i(R,t)$ were Fourier transformed to get $\eta_i(K,t)$. We got the corresponding spectral density of this wave of wavenumber K traveling in the ith antenna-look direction from the equation

$$F_i(K,t) = \frac{|\eta_i(K,t)|^2}{K \Delta K \Delta \phi_t}$$

where the $\Delta\varphi_t$ is the total angular resolution in K-space including antenna beamwidth, angular rotation during data collection and the azimuthal length of the resolution cell. This total angular resolution is given by (Plant et al., 1987)

$$\Delta\varphi_t = 4\sqrt{\ln 2}\left(\frac{2}{(KR\varphi_h)^2} + \frac{\varphi_n^2}{2}\right)$$

where

$$\varphi_n = \sqrt{\varphi_p^2 + (\Omega T_n)^2}$$

and

$$\varphi_p = \frac{\varphi_h}{\cos\theta_g \sqrt{2\ln 2}}$$

The brackets indicate an average over range, Ω is the antenna rotation rate in rad/sec and φ_h is the one-way, half-power, full antenna horizontal beamwidth. All angles are in radians.

Our two major assumptions are that the radar responds only to waves travelling along the radar's line of sight and that the Fourier components $\eta_i(K,t)$ are valid everywhere in the vicinity of the ship. With these assumptions, we can obtain the two-dimensional wave field around the ship as follows:

$$\eta(x,y,t) = \sum_i \sqrt{2}\, A_i(K,t) \cos(\mathrm{sgn}(K \cdot R)(K(x \sin\alpha_i + y \cos\alpha_i) + \varphi_i) - \omega_i t)$$

where x and y are coordinates in the east and north directions, α_i is the compass angle of the ith look direction, and ω_i is the angular frequency in the ith direction determined from the measured dispersion relation. The sign of the cosine of the angle between the antenna look direction and the direction of wave travel is indicated by $\mathrm{sgn}(K \cdot R)$. Also,

$$A_i(K,t) = \sqrt{\frac{F_i(K,t) K \Delta K \Delta\phi}{\Delta\phi_t}}$$

which is simply $|\eta(K,t)| \sqrt{\frac{\Delta\phi}{\Delta\phi_t}}$. The phase of η(K,t) is φ_i for the initial look in each direction.

An example of phase-resolved waves around the ship obtained by this procedure using 3.3 seconds of data (one interleaved rotation) is given in Figure 12. Again, the waves from the two methods are highly correlated but not precisely the same.

Because of our dealiasing, we can produce images such as those shown in Figure 12 every 1.1 seconds. Thus we can compare the time series of surface displacements from a spatial bin near the buoy with the time series of surface displacements from the buoy. Both the buoy and CORAR received a GPS signal so that time and location of CORAR and the buoy could be determined very accurately. We tracked the difference in the location of the buoy and the ship during the time of data collection and corrected for changes. We found that the change in separation was never more than one range cell in either the east or north direction. The buoy was located approximately at coordinates (60,-460) m in Figure 12. A comparison of various time series after location had been corrected is shown in Figure 13. Clearly the agreement between the various time series is not perfect but the correlations are sufficiently high to encourage development of this technique.

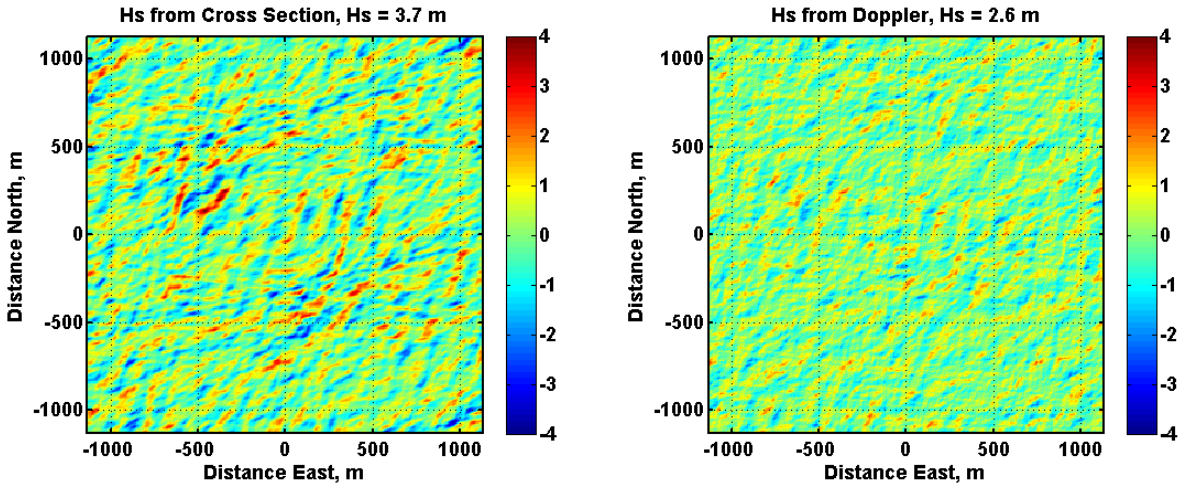

Figure 12. Phase-resolved waves around the R/V Thompson obtained from CORAR's received power (left) and Doppler offsets (right). Data were taken on August 13, 2008 at 17:56 UTC

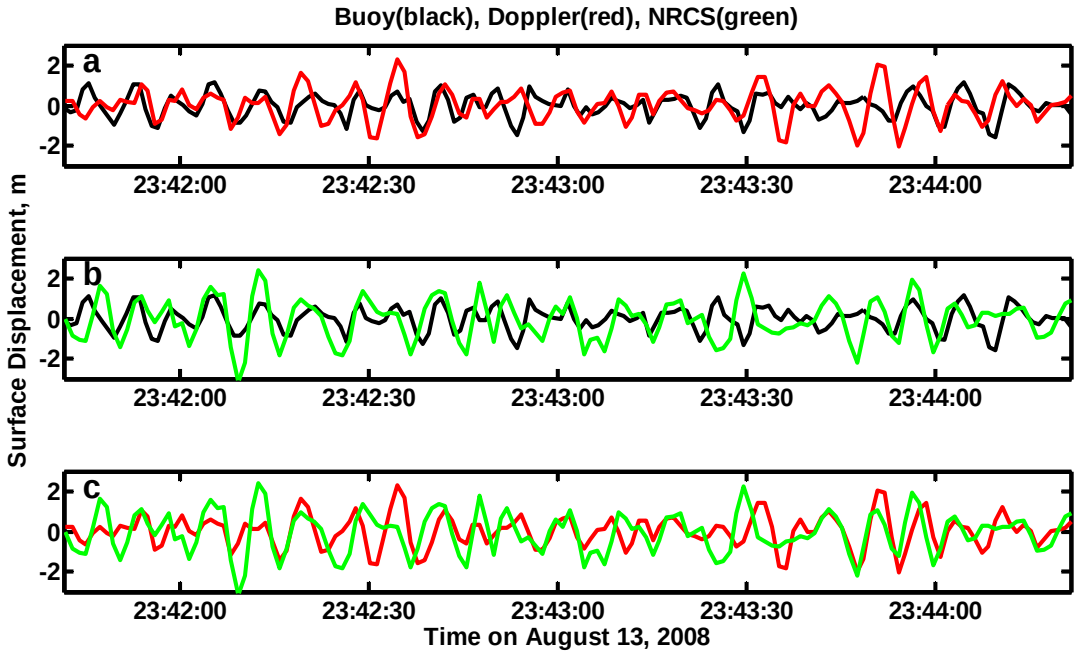

Figure 13. Comparison of various time series from CORAR and the buoy located at (60,-460) m in Figure 12 on August 13, 2012. a) Comparison of buoy wave heights (black) and those from Doppler shifts (red). b) Comparison of buoy wave heights and those from cross sections (green). c) Comparison of wave heights from Doppler shifts (red) and from cross sections (green).

Once the spectral densities of the waves in different look directions have been calculated, it is a simple matter to obtain the rms wave height by integration followed by temporal averaging. We did this for a set of our files taken 15 minutes apart. The averaging time was 54 seconds. Figure 14 shows the significant wave heights, H_s, obtained by multiplying these rms heights by 4

for 72 samples from August 13. The circles are from the NRCS, the asterisks are from the Doppler velocities, and the X's are from the buoys that were deployed on that day. A general trend of increasing H_s as the duration of wind speeds between 15 and 20 m/s increased is seen in the figure. However a significant decrease in wind speed and an accompanying small shift in wind direction occurred at about 8:00 UTC. A corresponding small dip in the significant wave height is observed at about this time.

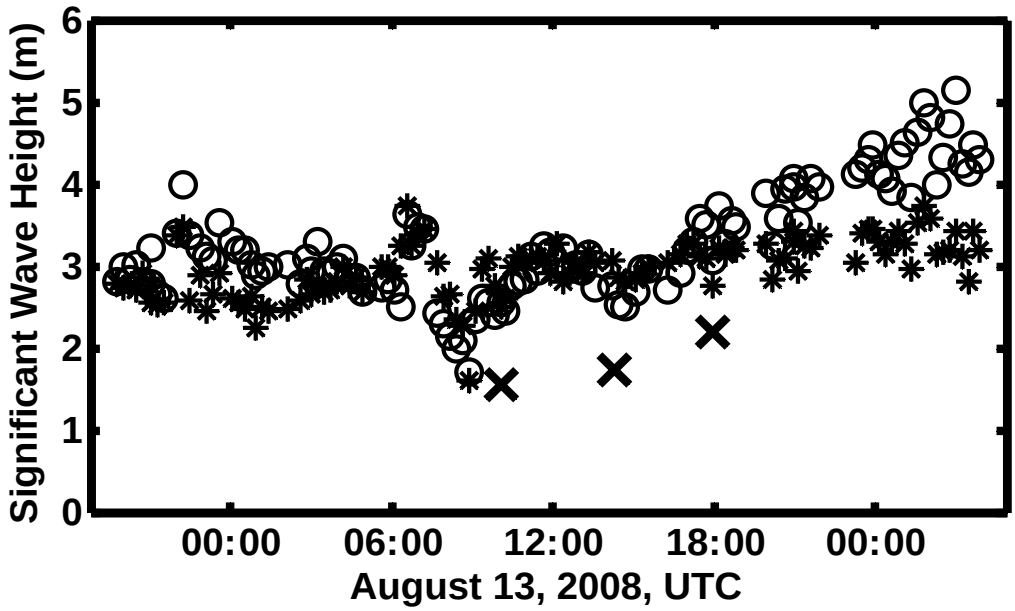

Figure 14. Significant wave heights, H_s, obtained from the phase-resolved wave fields measured by CORAR around the R/V Thompson on August 13. Asterisks show H_s from Doppler velocities, circles show H_s from the NRCS, and the X's show H_s measured by buoys that were tethered to the ship.

By plotting spectral densities in all look directions on a polar plot, averaging over all spectra obtained in our 162 second time record, and smoothing the resulting spectrum over four bins in range and azimuth, we produced the directional wave spectra shown in Figure 15a and 15b. Here, we have omitted the components of the spectra moving toward the radar and doubled those moving away. Thus, the spectra indicate the direction toward which the waves travel. The black lines in these panels give the wind direction; from the center out is the direction toward which the wind blows. By further integrating over azimuth angles, we produce the omnidirectional spectra shown in Figures 15c and 15d. These spectra are defined by

$$F(K) = \sum_i \{F_i(K,t)\}\Delta\phi$$

When multiplied by K and integrated over K, they yield the mean-square wave height. Four times the square root of this value is Hs given in the upper right corner of each plot. Hs from the buoy is also given there while the red curves in the lower panels show omnidirectional spectra from the buoy. Note that in converting these buoy spectra from frequency to wavenumber, the magnitude and direction of the current had to be known very accurately.

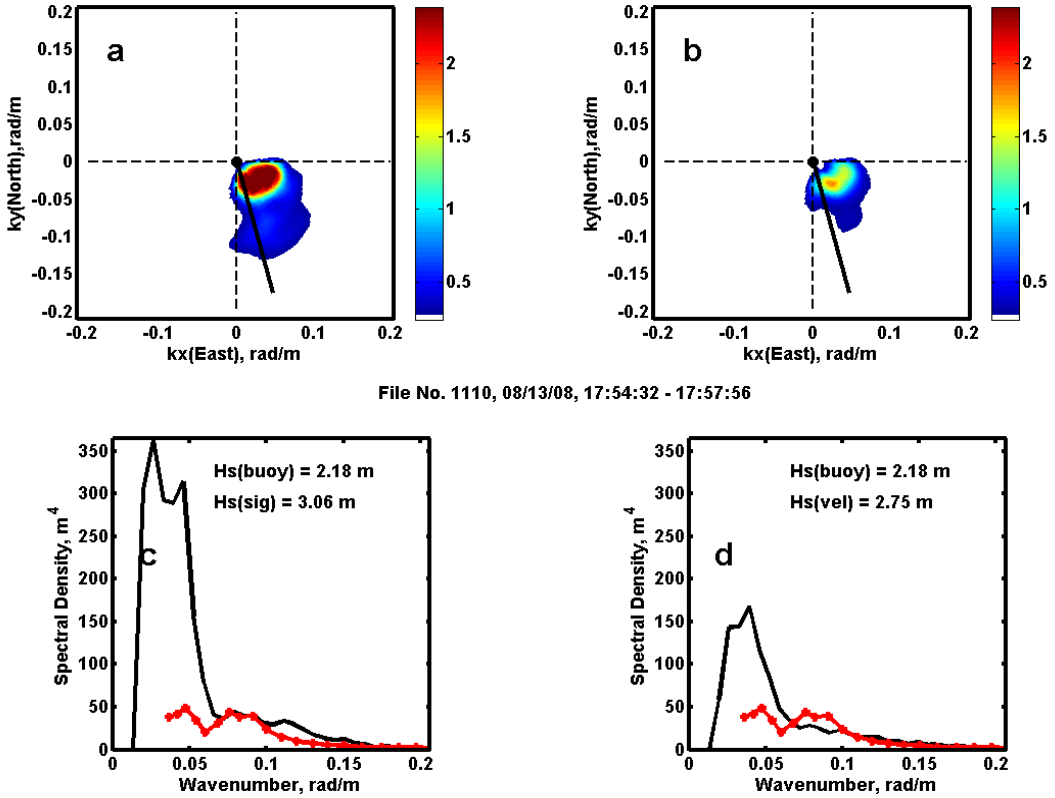

Figure 15. a) Directional wave spectra from cross sections. b) Directional wave spectra from Doppler shifts. c) Omnidirectional wave spectra from cross sections (black) and from the buoy (red). d) Omnidirectional wave spectra from Doppler shifts (black) and from the buoy (red). The black line in the upper panels show the direction toward which the wind blows, from the center out. Significant wave heights, H_s, are shown in the upper right corner of the lower panels. Data were taken on August 13, 2008 at 17:55 UTC.

We expect F(K) to depend on K approximately as K^{-4} at high wavenumbers so that the curvature variance spectrum in the wind direction, $K^4F_i(K)$, has a value between 0.001 and 0.002 for wavenumbers near 0.3 rad/m. This is usually called "α" since it is the same as the coefficient of the frequency spectrum first proposed by Phillips (1958). We attempted to determine the value of α from our spectra by using the multiscale model of Plant (1990) but adjusting the value of α to match our spectra at high wavenumbers. Figure 16 shows this fitting procedure and the values of α obtained. Figure 16a shows both wave height variance spectra (upper curves) and curvature variance spectra (lower curves). Solid curves are from Doppler velocities while dashed curves are from the NRCS. The vertical dotted line shows the wavenumber at which the radar-derived spectra were matched to spectra from the multiscale model. The figure shows that spectra from the NRCS are higher at low frequencies and lower at high frequencies than spectra from Doppler velocities. The K^{-4} spectrum also appears to provide a better fit to the high-wavenumber spectra from the Doppler velocities.

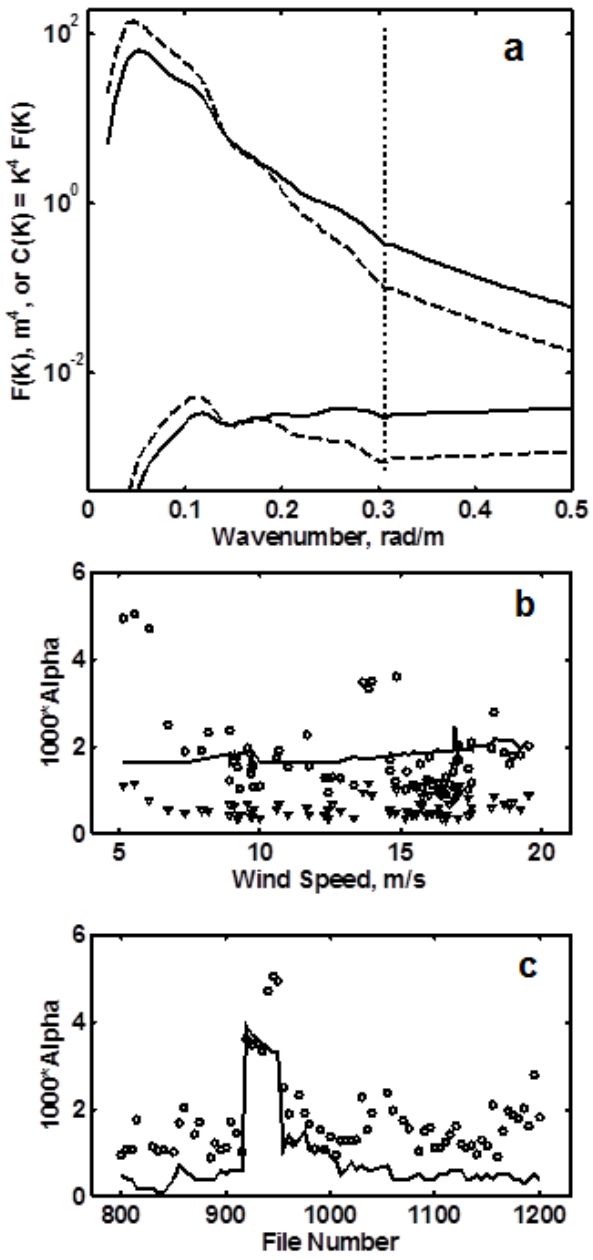

Figure 16. a) Wave height variance spectra integrated over azimuth (upper curves) and curvature variance spectra integrated over azimuth angle (lower curves). Solid curves are from Doppler and dashed curves are from cross section. Vertical dotted line shows the wavenumber at which radar spectra and theoretical spectra were matched. b) 1000 times Phillips' α versus wind speed. Circles are from Doppler, triangles are from cross section, and the line shows Banner's relation $\alpha = 0.0018\sqrt{\frac{U}{c_p}}$. c) Ship speed (solid curve) and α from Doppler offsets. Note the high α values when the ship speed was high.

Figure 16 b shows the values of α necessary to produce the fits shown in Figure 16a along with the values obtained from Banner's form, which may be written

$$\alpha = 0.0018 \sqrt{\frac{U}{c_p}}$$

where U is wind speed and c_p is the speed of the wave at the peak of the wavenumber spectrum derived from the radar-measured spectra (Banner, 1990). There are seven circles above α = 3 shown in Figure 16b. As Figure 16c shows, these all come from files where the ship speed was high. The reason for this is unknown but without these high values, the average α from Doppler shifts is 0.0015 while that from the cross sections is 0.0006. The mean of Banner's value of α over the range of wind speeds shown in Figure 16b is 0.0018. It appears that spectra from Doppler velocities yield better levels of the high-wavenumber spectrum than those from the NRCS.

Conclusions

We have shown that winds, waves, and currents can all be measured by a coherent shipboard radar operating at vertical polarization and low-grazing angles.

Currents were probably the most accurate of the quantities measured by the radar. These were determined by fitting the first-order surface wave dispersion relation to measurements along a series of azimuth angles by varying the current component along each azimuth angle. The resulting currents tracked current components measured by the shipboard pitot tube to within a few cm/s.

We showed that these currents could not explain the frequencies of the centroids of the Doppler spectra measured by the coherent radar. These centroids were at frequencies that implied much larger velocities as their cause, and velocities that were larger looking upwind than downwind. We believe that these large Doppler offsets are a manifestation of the correlation between wave-induced backscattered power and wave-induced Doppler shifts, as first described by Hasselmann and Schieler (1970), probably augmented by breaking wave effects. Raster scans of Doppler spectra from a CW microwave system illuminating a small spot on the sea surface clearly illustrate this effect (Keller et al., 1986).

Winds measured around the ship by the radar tracked those measured by the ship's anemometer with rms accuracies reminiscent of early satellite scatterometer winds. The rms difference in speed was 2.8 m/s and that in direction was 18^o. While these are not as small as one might wish, we believe that the use of antennas with somewhat wider vertical beamwidths could improve the numbers. Transmitting more power should also help.

Finally we showed that both phase-resolved wave fields and the statistical properties of these fields could be measured within an area approximately 2.2 km on a side using both measured Doppler shifts and measured cross sections. These agreed, again, reasonably well with similar quantities measured at a single point by a buoy. The primary assumptions used to compute these

wave fields from the radar return were that the radar responded only to waves travelling very close to its look direction, that measured Fourier components were valid everywhere around the ship, and that the wave-induced variations in NRCS were primarily due to local changes in grazing angle. For the longer waves, the unidirectional assumption may break down, although it appeared to be accurate at least up to the 100 m waves encountered in our experiments. In general, wave spectra from Doppler shifts seemed to fit buoy spectra better than did wave spectra from cross sections, being better fits at both low and high wavenumbers. Interestingly, however, phase-resolved surface displacements from cross sections were somewhat more correlated with those measured by the buoy than were surface displacements from Doppler shifts. However, it is well known that the MTF is large at low wavenumbers and low at high wavenumbers. Therefore, the higher correlations for wave heights from the NRCS could simply be due to this effective smoothing by the MTF since it has not been removed in our work

We note that our technique is quite different from the technique often used to retrieve phase-resolved wave heights from marine radar images. These often use data from only small rectangles in the radar image, obtaining spectra through Fourier transforms and wave heights via a modulation transfer function. These techniques can respond only weakly to waves travelling perpendicular to the mean look direction of the rectangle for three reasons. First, all phenomena that produce wave-induced variations of the received power and radial velocity are much weaker for waves travelling perpendicular to the antenna look direction. Second, even though a marine radar has a very narrow beamwidth, it is not infinitely narrow so it produces some K-space angular discrimination against waves travelling perpendicular to the look direction. Finally, all these techniques filter around the dispersion relation, which rather efficiently discriminates against waves travelling perpendicular to the look direction. For these reasons, a technique which utilized data from only a small part of the radar image cannot capture waves travelling perpendicular to the mean antenna-look direction of this part. Since mixed seas are the rule rather than the exception on the ocean, this technique cannot produce correct wave heights most of the time.

While none of the radar measurements reported here agreed perfectly with those from more standard instruments, the agreement was sufficiently promising to encourage continued development of the radar techniques. We are in the process of making improvements to the radar that we hope will lead to winds, waves, and currents that more closely agree with in situ measurements.

References

Banner, M.L., Equilibrium spectra of wind waves, J. Phys. Ocean., 20, 966-984, 1990.

Chang, M-H, R-C Lien, Y.J. Yang, T.Y. Tang, and J. Wang, A Composite View of Surface Signatures and Interior Properties of Nonlinear Internal Waves: Observations and Applications, J. Atmos. Ocean. Tech., 25, 1218 – 1227, DOI: 10.1175/2007JTECHO574.1, 2008.

Dankert, H., J. Horstmann, and W. Rosenthal, Wind- and Wave – Field Measurements Using Marine X-Band Radar-Image Sequences, J. Ocean. Eng., 30(3), 10.1109/JOE.2005.857524, 534–542, 2005.

Dankert, H., and W. Rosenthal, Ocean surface determination from X-band radar-image sequences, J. Geophys. Res., 109, C04016, doi:10.1029/2003JC002130, 2004.

Hara, T. and W.J. Plant, Hydrodynamic modulation of short wind-wave spectra by long waves and its measurement using microwave backscatter, J. Geophys. Res., 99 (C5), p. 9767-9784, 1994.

Hasselmann, K., and M. Schieler, Radar backscatter from the sea surface, Eighth Symp. On Naval Hydro., Rome, Italy, 361-388, 1970.

Jones, W.L., L. C. Schroeder, and J. L. Mitchell, "Aircraft measurements of the microwave scattering signature of the ocean," J. Oceanic Eng., vol. OE-2, pp. 52-61, 1977.

Keller, W.C., W.J. Plant, and G.R. Valenzuela, Observations of breaking ocean waves with coherent microwave radar, in Wave Dynamics and Radio Probing of the Ocean Surface, ed. O.M. Phillips and K. Hasselmann, Plenum Publishing Corp., 285-293, 1986.

Keller, W.C., and W.J. Plant, Cross sections and modulation transfer functions at L- and Ku-Bands measured during the TOWARD experiment. J. Geophys. Res., 95 (C9), 16,277-16,289, 1990.

Nieto Borge, J.C., G.R. Rodriquez, K. Hessner, and P. I. Gonzalez, Inversion of Marine Radar Images for Surface Wave Analysis, J. Atmos. Ocean. Tech., 21, 1291-1300, 2004.

Phillips, O.M., The equilibrium range in the spectrum of wind-generated ocean waves, J. Fluid Mech., 4, 426-434, 1958.

Plant, W.J., W.C. Keller, A. Cross, Parametric dependence of ocean wave-radar modulation transfer functions. J. Geophys. Res., 88(C14), 9747-9756, 1983.

Plant, W.J., W.C. Keller, A.B. Reeves, E. Uliana, and J.W. Johnson, Airborne microwave Doppler measurement of ocean wave directional spectra, Intl. J. Remote Sensing, 8 (C3), 315-300, 1987.

Plant, W. J., W. C. Keller, V. Hesany, and K. Hayes, Measurements of the marine boundary layer from an airship, J. Atmos. Oceanic Technol., 15, 1433–1458, 1998.

Plant, W.J., A stochastic, multiscale model of microwave backscatter from the ocean, J. Geophys. Res.,107(C9), 3120, doi:10.1029/2001JC000909, 2002.

Plant, W. J., W. C. Keller, K. Hayes, and G. Chatham, Normalized radar cross section of the sea for backscatter: 1. Mean levels, J. Geophys. Res., 115, C09032, doi:10.1029/2009JC006078, 2010.

Plant, W.J. and G. Farquharson, Origins of features in wavenumber-frequency spectra of space-time images of the ocean, J. Geophys. Res., 117, C06015, doi:10.1029/2012JC007986, 2012.

Plant, W.J., Whitecaps in deep water, Geophys. Res. Ltrs., 39, L16601, doi:10.1029/2012GL052732, 2012.

Pulse Width (nsec)	50
Pulse Width (MHz)	20
Pulse Width (m)	7.5
Pulse Rate (Hz)	50000
Rate per Antenna (Hz)	25000
Time between pulses (μsec)	20.0
Max possible number of range bins	400
Number of range bins used	252
Number of Pulses Collected	1024
Number of Pulses Averaged	16
Time to Collect Samples (msec)	41.0
Time for Calculations (msec)	10
FFT Size	64
Sample Rate (Hz)	1562.5
Frequency Resolution (Hz)	24.4
Nyquist Freqency (Hz)	781.3
Rotation Period (sec)	13.2
Rotation Rate (deg/sec)	27.3
Rotation Azimuthal Resolution (deg)	1.1
Antenna Length (feet)	2.0
2-Way Horizontal Antenna Beamwidth (deg)	2.6
Antenna Width (feet)	2.0
2-Way Vertical Antenna Beamwidth (deg)	2.6
Antenna Gain (dB)	34.9
Total Azimuthal Resolution (deg)	3.7
Maximum Range (km)	1.9
Azimuthal Width at Maximum Range (m)	123

Table 1. Specifications of the APL/UW COherent Real Aperture Radar (CORAR)

Coherent Marine Radar Measurements of Directional Wave Spectra Using Vertically Polarized Antennas

Dennis B Trizna
Imaging Science Research, Inc.
6103B Virgo Court
Burke, VA 22015 USA

Abstract- ***A coherent marine radar has been developed for imaging ocean wave orbital wave velocity wave patterns. A NOPP program, Roadmap: Technologies for Cost Effective, Spatial Resource Assessments for Offshore Renewable Energy, has helped finance recent ISR studies. This new coherent radar provides a direct measurement of ocean wave orbital wave velocity without relying on a modulation transfer function (MTF) that has been used with previous systems that map radar echo intensity. The latter approach is prone to error due to environmental dependencies of the MTF, particularly when winds blow into incoming waves, which then produces an enhanced echo strength that is misinterpreted by the MTF scaling as due to larger wave slopes and heights. With this new direct measurement of orbital wave velocity, directional ocean wave spectra can be measured unambiguously, and deterministic ocean wave height fields that can be mapped for real-time input into wave forecasts for ship motion response applications. Results of experiments conducted at the USACE pier in Duck, NC, during the passage of Hurricane Irene are presented, showing the effect of using vertically polarized antennas, minimizing wave breaking effects for wave heights above 2.5 m.***

I. OMEGA-K SPECTRA

Marine radar offers a snapshot sequence every 1.25 to 2.5 s of the coastal wave field that can be used for the application of a number of image processing algorithms. A number of researchers have established the utility of using both radar and optical video image sequences to derive useful coastal ocean properties from such data [1-7]. We fave recently developed an integrated radar and data acqusition package to make such measurements synoptically and unattended. The prototype system has been set up at the U.S. Army Corps of Engineers Field Research Facility (FRF), Duck, NC for extensive testing and ground truth comparison. Real time results can be viewed at the FRF website (frf.usac.army.mil/radar). The coherent marine radar processing is very similar to that of the non-coherent version, as maps of ocean waves are also created. However, in the case of the standard marine radar, the image is one of backscatter intensity. For the coherent marine radar, the image will be the radial component of orbital wave velocity, that will represent traveling ocean wave orbital wave velocity maps. As the processing is similar for both cases, we first present the general approach used for the standard marine radar.

II. COHERENT RADAR DESCRIPTION

Use of non-coherent marine radar for ocean wave spectra measurement is feasible by making use of multiple-rotation images, and 3-D FFT image processing to derive Ω-K ocean wave spectra. We have developed a similar capability, based on the Sitex family of marine radars. The coherent radar has a similar look to standard marine radars, as seen below, for such a system currently operating at the USACE Field Research Facility, at Duck NC shown in Fig. 1 below.

Figure. 1. ISR coherent marine radar used for wave sensing.

The radars used for the results presented here are two . The first is our coherent-on-receive ISR CORrad Digital Imaging Radar Model 25.9, based on a modified Koden 25-kWatt 9' antenna system, with our digital acquisition system and signal processing systems, Radar Image Processing Suite (RIPS). A fully coherent prototype radar (COHrad) was developed in house, and a new solid state transceiver just delivered for our commercial version. With suitable processing, the COR IF signal can be used to retrieve coherent estimates of radial velocity similar to CORrad, as will be demontrated later.

The radar makes use of pulse compression to achieve improved gain over the standard marine radar, allowing it to operate with just 5-watts of peak power. A 1-μs pulse that is transmitted is shown in Fig. 2a below, chirped over 30 MHz in this case, and mixed up to X-band for transmission. Echoes have a similar shape and pulse compression correlation creates in-phase (I) and quadrature (Q) samples that are used for velocity measures. These are shown in Fig.

2b and 2c below.

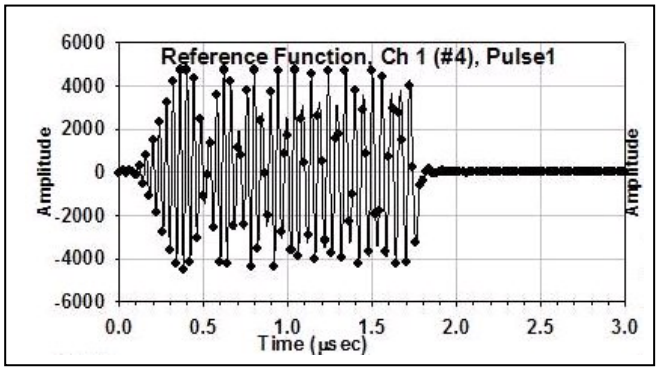

Figure 2a. Chirped pulse transmitted, after mixing to X-band.

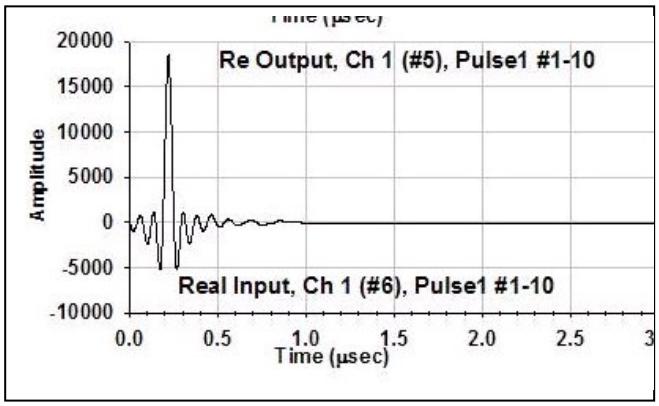

Figure 2b. In-phase pulse compressed echo using 2a.

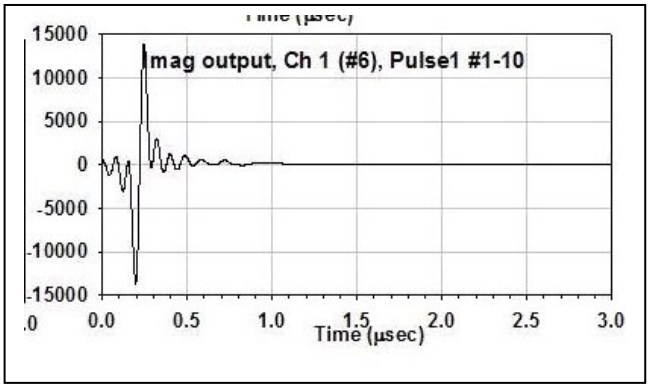

Figure 2c. Quadrature signal (90 deg out of phase with I).

The phase at each time sample is determined from the equation ATAN(I/Q), and a phase difference, dϕ, from two consecutive pulses is calculated for each range sample. This is proportional to the radial velocity using the Doppler equation, $v = d\phi / (\lambda/2)$. The range-azimuth matrix of radial velocities are then transformed into Cartesian co-ordinates for each rotation of the radar. The radar video echo intensity signal, $S(R.\phi)$, can be formed at each pixel for comparison using $S(R.\phi) = (I^2+Q^2)^{1/2}$. A map of images of intensity and radial velocity is shown below in Fig. 3a and 3b.

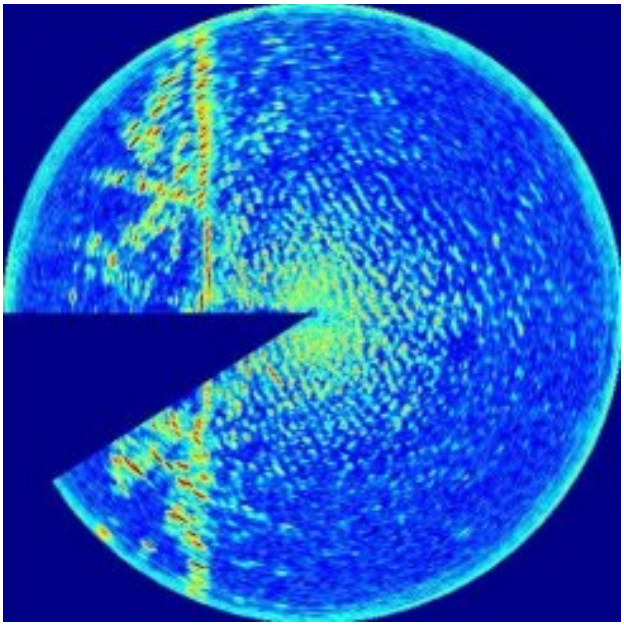

Figure 3a. Radar echo intensity image.

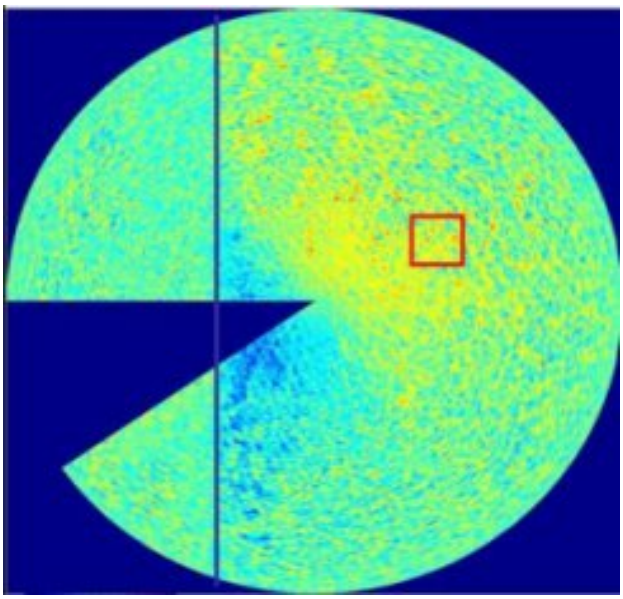

Figure 3b. Radial velocity image.

The radial velocity map appears to show usable information at ranges where the intensity signal is weak, but stil provides quality I/Q values to allow phases to be determined. There is an offset due to current here that will be discussed later. The red box represents a user-selectable set of pixels that can be chosen for successive rotations to be used as input to a 3D-FFT analysis that is used to determined values of spectral samples of waveheight-squared/Hz. This window can be moved about the radar coverage scene to study wave dissipation, for example, or wave refraction spectra in unusual bathymetry environments. One must correct for the radar aspect relative to the primary

wave direction, as the radar radial component will vary like cosine of the difference of wave travel vs radar illumination.

III. OMEGA-K SPECTRA

Fig. 4 represents a subset of frequency spectra from a set of 32 that are available when using 64 rotations of 64x64 pixels, then averaging over 8 of such sets covering a 10-min period. The yellow circle seen represents the shallow water dispersion rule for the depth chosen, 10 m, while the red circle represents deep water.

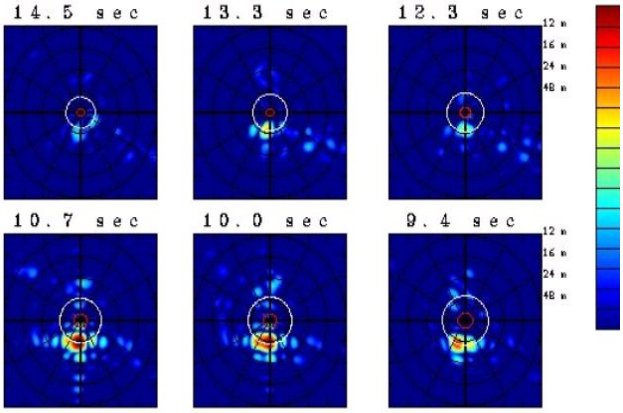

Figure. 4. K_x-K_y Spectra at each of a series of wave frequencies from the Ω-K spectral analysis.

The spectral peaks clearly lie on the shallow water dispersion circle chosen, and each image can be filtered using a band between 80% and 120% of this radius, to account for tidal changes in depth. All energy in this band will represent samples of wave height squared per unit Hz, (0.4Hz/64 in this case). This is obtained by relating the radial velocity from the radar measure to the spectral waveheight component using the time derivative of the equation defining the x-position of a patch of water on a wave surface :

$$X(t) = (H/2)\cos(\Omega t) \qquad (1)$$

In the case of processing the intensity image of a standard marine radar, similar image intensity spectra result, but each radar frequency component must be scaled to some surface truth representation of the weave frequency spectrum using an emprical constant, a spectral Modulation Transfer Function. This has shown to be in error when environental conditions change (wind direction relative to wave direction, for example), and if the radar modulator ages with time and exhibits chaning output power. The coherent radar approach requires no such scaling, and is independent of such environmental factors. A patent based on this approach has been applice for by ISR and is pending, and an international provisional patent has also been filed.

IV. FREQUENCY SPECTRA AND H_m0

If one sums the spectral energy in the band about the shallow water dispersion relation for each of 32 windows, one derives an omni-directional freqeuency spectrum. A comparison of that derived from coherent radar data over 10 minutes, and the pressure array sensor at the FRF for two overlapping periods of 3-hr each is shown in Fig. 5 below.

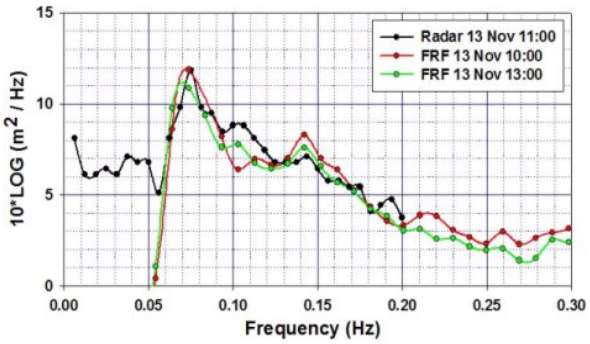

Figure 5. Frequency spectra from COHrad and FTF pressure array.

If one sums the energy from each spectral peak in the frequency spectrum above, one forms H_m0, a RMS waveheight estimate. Examples of results of H_m0 comparisons are now made for both horizontal and veritical antenna polarization cases.

V. H-POLARIZATION : HURRICANE IDA

During November of 2009, Hurricane Ida passed offshore of the FRF site and waves of 4-m were observed. Below are plotted the time series of H_m0 from the radar vs that from the FRF pressure sensor array.

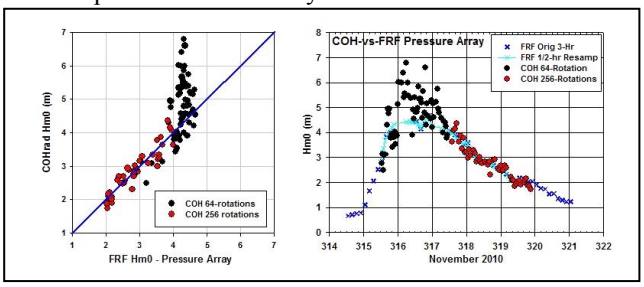

Figure 6. Hm0 time series from radar vs FRF pressure array compared.

The black circles represent very short times of collections, just 64 rotations covering ~2.5 minutes, enought for a single 3D-FFT analysis. As the winds subsided but the waves still being high, the collections were increased to 256 rotations, represented by the red circles. The initial interpretation of these outliers for waves 4-m and higher was that insufficient time was used for the data collection periods. These data were collected looking directly offshore into the onshore advancing long waves from the storm. An analysis was performed for look angles of the 64x64 pixel analysis

window further north, and it was found that the outliers were reduced in number. The outliers reduced in number for other windows chosen further left of off-shore. This suggested that perhaps breaking waves offshore for the highest wave conditions were causing anomolous contributions to the radial velocity, causing an enhancement in the radar derived wave height estimates. The gtreatest effect breaking waves will have in echo amplitude will be when illuminated nearly perpendicular to the breaking wave face or edge [8].

A Coherent-on-Receive radar (CORrad) was run during the same time from the same location a frew meters away, and processing that data in a similar fashion produced results for H_m0 as well. These are shown in Fig. 7 below, also using a horizontally polarized antenna.

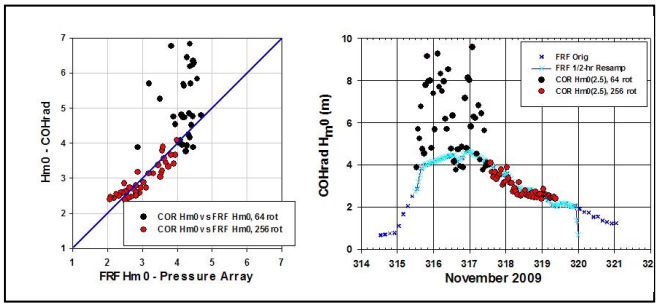

Figure 7. CORrad Hm0 vs FRF pressure array results

The results from the CORrad system are quite similar to those of the COHrad for the same period, and the same outlier behavior is seen for waves above 4 meters.

VI. V-POLARIZATION: HURRICANE IRENE

In the summer of 2011, Hurricane Irene passed the Outer Banks inland of our radar site, but waves generated earlier while the storm was still offshore generated 4.2 m waves at the FRF pier. In preparation for this storm, the COHrad antenna was switched from a 9' horizontally polarized antenna to a 4' vertically polarized unit. The hypothesis to explain the outliers seen in the previous figures was that for very high waves, severe spilling breakers were occurring in far deeper water than under lower wave conditions, and the acceleration of wave breaking crests under such conditions might be biasing the radial velocity measurements made with horizontal polarization. In a previous work [8], we showed the dramatic difference between low grazing angle images for HH and VV polarization. For HH, small scale breaking features dominate the scene, with their azimuthal echo strength dependence falling off when illuminated further off normal to the breaking edge. This behavior suggested a scattering width of about 25 cm for the small pancake breakers that were observed visually, with virtually no echo when seen from a direction illuminating the back of these waves, opposite the wind. For VV, these discrete echoes do not appear, and distributed Bragg sources dominate the scattering process, with a modest front-to-back ratio of 6 dB or so when looking into the wind versus opposite it. This suggests that a vertically polarized antenna might eliminate outliers due to breaking wave crests of a much larger scale than observed in [8].

Figure 8 shows a time series of Hm0 measured using COHrad with the V-pol antenna for wave conditions up to 4.2 m. The outliers that occurred previously are not seen here.

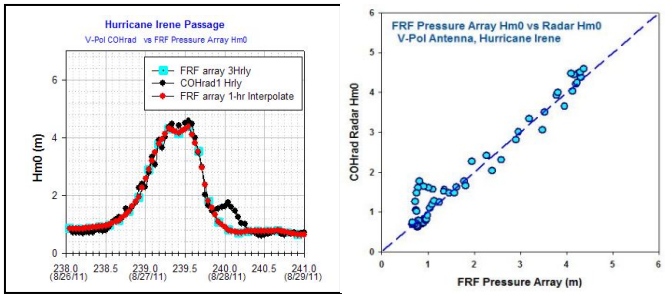

Figure 8. COHrad data during Irene with a V-pol antenna.

For the same time, a CORrad was run with an H-pol antenna, covering the same period of collection and location at the end of the FRF pier. There were outliers in these data, starting at about the same Hm0 value as in figures 6 and 7 above. Thus, we feel that our hypothesis has been validated, that outliers for high sea states above 3.5 m or so will generate errors in H_m0 retrieval. However, as small scale breaking allows one to image the location of the offshore bar, as we have shown previously, there may be a trade off in keeping an H-pol antenna for coastal sites, where the very high sea conditions are rarely encountered, but bard imaging is important. We have not yet compared the sensitivity between the two polarizations for very weak wave conditions, where H-pol might provide a reasonable echo for other applications as well. The agreement for the 0.4-m minima seen in Figure 8 do suggest that the ability to retrieve wave spectra for small waves is not hampered severely.

VIII. SUMMARY

We have demonstrated the use of a newly designed coherent marine radar to measure directional wave spectra and surface radial currents. Data were compared with surface truth instrumentation from the USACE Field Research Facility, both pressure array sensor data for wave height, and AWAC acoustic sensors. Data from a coherent-on-receive radar that was run simultaneousl from the end of the pier at the FRF and compared favorably as well. Both types of radars operting with horizontally polarized antennas produced excessively high H_m0 retrievals for wave heights above 2.5 meters, when the analysis window was directly offshore, and radar illumination was directly into

the advancing sominant waves, which were breaking for this limit. The hypothesis was mde that these outliers were caused by breaking wave crest accelerations that were hight than the orbital wave velocity of these dominant waves. Only for waves 2.5 m and higher does breaking occur in the deeper waters used for the analysis. A vertically polarized antenna was used duing the passage of Hurricane Irene, and the outlier effect was not observed, confirming our hypothesis. The choice of polarization will depend on the emphasis of the type of output required. I.e., if accurate wave spectra are desired, vertical polarization should be used. If bar location and mapping is the prime product, then horizontal polarization should be used, as small scale breaking produces a

For this location, we have shown previously [10] that surface currents along shore can be measured reasonably accurately for the modest radar height of roughly 11 m, as the radar is looking along the crests and troughs and does not suffer shadowing, even for modest to low radar height for this geometry. Looking offshore, the troughs would be shadowed by the crests for very steep waves, and the orbital wave velocity would not present a zero mean to the radar look. We found this to be the case for a shore based radar on another occasion, where the currents were in error due to crest orbital wave influences. For this case, the wave height analysis was still quite respectable. On more recent observations at other sites with radar heights ranging from 19 m to 26 m, no shadowing was encountered and long range currents could be measured accurately.

A pair of radars discussed here, placed of the order of 300 to 1,000 m apart, should be able to provide a vector map of surface currents at 3-m resolution. Such a method should be useful for detection of rip currents and riverene flow, in addition to currents in harbors for ship traffic application.

ACKNOLEDGEMENTS

We wish to acknowledge the data provided by the USACE FRF, in particular, to Kent Hathaway who extracted the data from historical records that allowed the comparisons to be made on a timely basis. ISR has a continuing Co-operative R&D Agreement with the FRF.

REFERENCES

[1] H. Dankert J. Horstmann, and W. Rosenthal, Ocean Wind Fields Retrieved from Radar-Image Sequences, J. Geophys. Res.. Vol. 108, 2005.

[2] I.R.Young, , W. Rosenthal, F. Ziemer, A three-dimensional analysis of marine radar images for the determination of ocean wave directionality and surface currents, JGR, **90**, C1, pp. 1049-1059, 1985.

[3] D.B. Trizna, "Errors in Bathymetric Retrievals using Linear Dispersion In 3D FFT Analysis of Marine Radar Ocean Wave Imagery," IEEE Trans. Geosciences and Remote Sensing, **39**, pp. 2465-2469, 2001.

[4] C.M. Senet, J. Seemann, F. Ziemer, An iterative technique to determine the near surface current velocity from time series of sea surface images, Oceans '97, Halifax, 1997.

[5] Dugan, J.P., H.H. Suzukawa, C.P. Forsythe, M.S. Farber, Ocean wave dispersions surface measured with airborne IR imaging system, IEEE Trans. Geosciences and Remote Sensing, **34**, pp. 1282-1284, 1996.

[6] Dugan, J.P., C.P. Forsythe, H.H. Suzukawa, M.S. Farber, Bathymetry estimates from long range airborne imaging systems, Proc. 4th Int. Conf. On Remote Sensing for Marine and Coastal Environments, Orlando FL, 1997.

[7] Stockdon, H.F., and R.A. Holman, Estimation of wave phase speed and nearshore bathymetry from video imagery, J. Geophysical Res., **105**, pp. 22,015-22,034, 2000.

[8] McGregor, J.A., E.M Poulter, M.J. Smith, Switching system for single antenna operation of an S-band FMCW radar, IEE Proc. –Radar, Sonar, Navig, Vol. 141, pp 241-248, 1994.

[9] Trizna, D.B., and D. Carlson, Studies of low grazing angle radar seascatter in nearshore regions, IEEE Trans. Geosciences and Remote Sensing, **34**, pp. 747-757, 1996.

[10] Trizna, D.B., Coherent Marine Radar Measurements of Ocean Surface Currents and Directional Wave Spectra, Oceans 2011, Santander Spain, 6-10 June 2011.

Coherent Marine Radar Measurements of Ocean Surface Currents and Directional Wave Spectra

Dennis B Trizna
Imaging Science Research, Inc.
6103B Virgo Court
Burke, VA 22015 USA

***Abstract*- A coherent marine radar with 3-m resolution has been developed that measures the radial component of the orbital wave velocity of ocean waves, as well as the mean radial ocean surface velocity. This radar allows direct measurement of the ocean wave spectrum by means of 3D-FFT processing of a sequence of coherent radar images of orbital wave patterns. Currently, with a 2.5-s rotation rate, 256 images cover a period of the order of ten minutes, with frequency alias at 0.2 Hz, with upgrade to 0.4 Hz planned with later units. Radial current maps are obtained by a superposition of all radial velocity images collected. This summing forces orbital wave patterns to blend to the mean, resulting in the map of mean radial current. A pair of such radars operated at a coastal site, separated by a few hundred meters along the coastline, may allow the combination of 2-site radial components to be combined into a mean current vector field. Results of first tests of the first prototype radar measurement of radial current and RMS wavehieght are presented for a field site at the U.S. Army Corps of Engineers Field Research Facility, Duck, N.C.**

I. OMEGA-K SPECTRA

Marine radar offers a snapshot sequence every 1.25 to 2.5 s of the coastal wave field that can be used for the application of a number of image processing algorithms. A number of researchers have established the utility of using both radar and optical video image sequences to derive useful coastal ocean properties from such data [1-6]. We fave recently developed an integrated radar and data acqusition package to make such measurements synoptically and unattended. The prototype system has been set up at the U.S. Army Corps of Engineers Field Research Facility (FRF), Duck, NC for extensive testing and ground truth comparison. Real time results can be viewed at the FRF website (frf.usac.army.mil/radar). The coherent marine radar processing is very similar to that of the non-coherent version, as maps of ocean waves are also created. However, in the case of the standard marine radar, the image is one of backscatter intensity. For the coherent marine radar, the image will be the radial component of orbital wave velocity, that will represent traveling ocean wave orbital wave velocity maps. As the processing is similar for both cases, we first present the general approach used for the standard marine radar.

II. COHERENT RADAR DESCRIPTION

Use of non-coherent marine radar for ocean wave spectra measurement is feasible by making use of multiple-rotation images, and 3-D FFT image processing to derive Ω-K ocean wave spectra [1-7]. We have developed a similar capability, based on the Sitex family of marine radars. The coherent radar has a similar look to standard marine radars, as seen below, for such a system currently operating at the USACE Field Research Facility, at Duck NC shown in Fig. 1 below.

Figure. 1. ISR coherent marine radar used for wave sensing.

The radars used for the results presented here are two . The first is our coherent-on-receive ISR CORrad Digital Imaging Radar Model 25.9, based on a modified Koden 25-kWatt 9' antenna system, with our digital acquisition system and signal processing systems, Radar Image Processing Suite (RIPS). A fully coherent prototype radar (COHrad) was developed in house, and a new solid state transceiver just delivered for our commercial version. With suitable processing, the COR IF signal can be used to retrieve coherent estimates of radial velocity similar to CORrad, as will be demontrated later. A photo of the solid state module, including 5-watt power amplifier, is shown in Fig. 2.

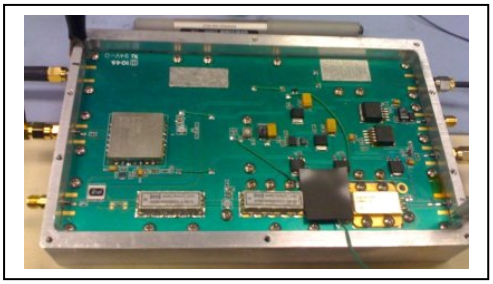

Figure 2. Solid state transceiver module.

The radar makes use of pulse compression to achieve improved gain over the standard marine radar, allowing it to operate with just 5-watts of peak power. A 1-µs pulse that is transmitted is shown in Fig. 3a below, chirped over 30 MHz in this case, and mixed up to X-band for transmission. Echoes have a similar shape and pulse compression correlation creates in-phase (I) and quadrature (Q) samples that are used for velocity measures. These are shown in Fig. 3b and 3c below.

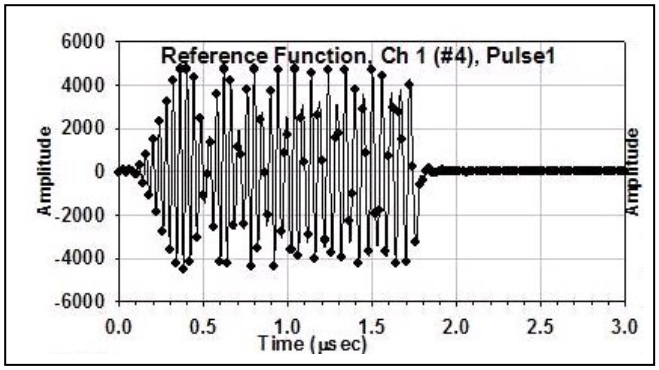

Figure 3a. Chirped pulse transmitted, after mixing to X-band.

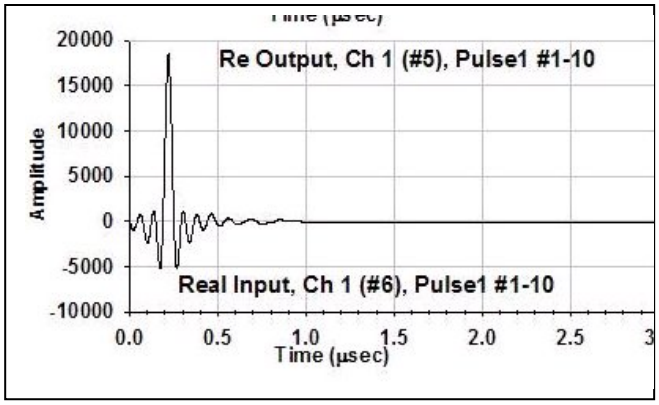

Figure 3b. In-phase pulse compressed echo using 3a.

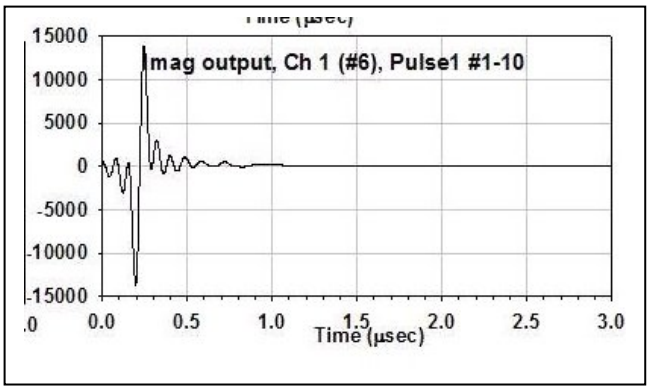

Figure 3c. Quadrature signal (90 deg out of phase with I).

The phase at each time sample is determined from the equation ATAN(I/Q), and a phase difference, dϕ, from two consecutive pulses is calculated for each range sample. This is proportional to the radial velocity using the Doppler equation, $v = d\phi / (\lambda/2)$. The range-azimuth matrix of radial velocities are then transformed into Cartesian co-ordinates for each rotation of the radar. The radar video echo intensity signal, $S(R.\phi)$, can be formed at each pixel for comparison using $S(R.\phi) = (I^2+Q^2)^{1/2}$. A map of images of intensity and radial velocity is shown below in Fig. 4a and 4b.

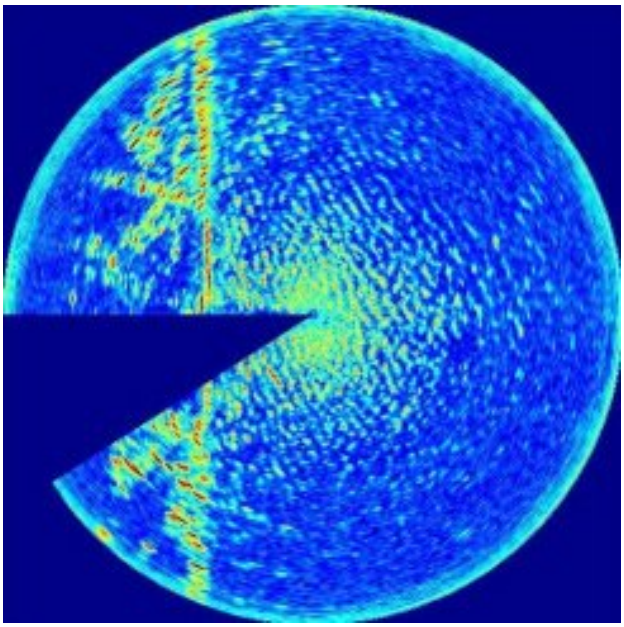

Figure 4a. Radar echo intensity image.

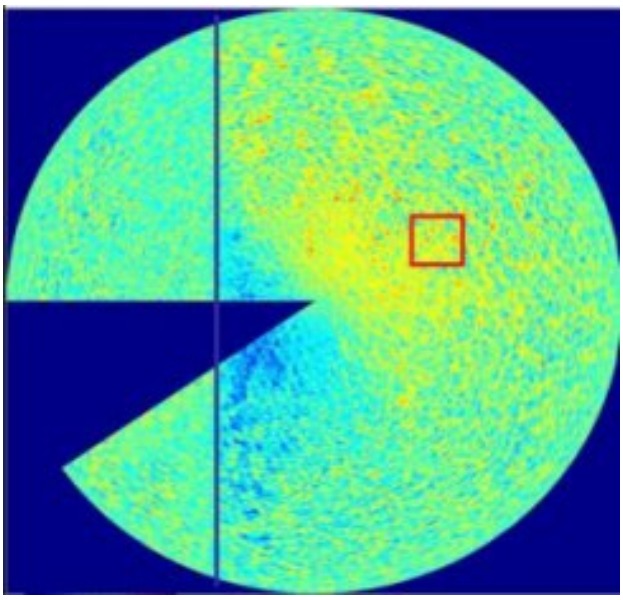

Figure 4b. Radial velocity image.

The radial velocity map appears to show usable information at ranges where the intensity signal is weak, but stil provides quality I/Q values to allow phases to be determined. There is an offset due to current here that will be discussed later. The red box represents a user-selectable set of pixels that can be chosen for successive rotations to

be used as input to a 3D-FFT analysis that is used to determined values of spectral samples of waveheight-squared/Hz. This window can be moved about the radar coverage scene to study wave dissipation, for example, or wave refraction spectra in unusual bathymetry environments. One must correct for the radar aspect relative to the primary wave direction, as the radar radial component will vary like cosine of the difference of wave travel vs radar illumination.

III. OMEGA-K SPECTRA

Fig. 5 represents a subset of frequency spectra from a set of 32 that are available when using 64 rotations of 64x64 pixels, then averaging over 8 of such sets covering a 10-min period. The yellow circle seen represents the shallow water dispersion rule for the depth chosen, 10 m, while the red circle represents deep water.

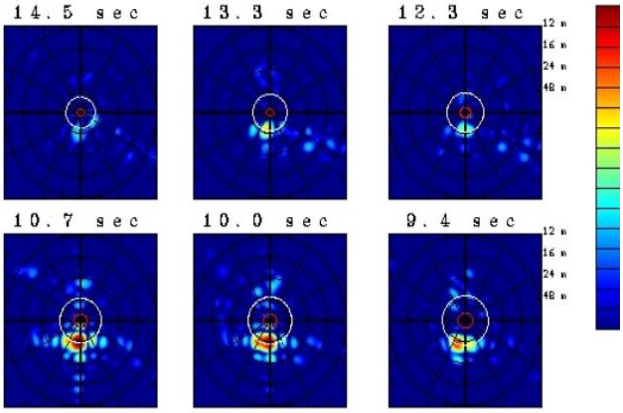

Figure. 5. K_x-K_y Spectra at each of a series of wave frequencies from the Ω-K spectral analysis.

The spectral peaks clearly lie on the shallow water dispersion circle chosen, and each image can be filtered using a band between 80% and 120% of this radius, to account for tidal changes in depth. All energy in this band will represent samples of wave height squared per unit Hz, (0.4Hz/64 in this case). This is obtained by relating the radial velocity from the radar measure to the spectral waveheight component using the time derivative of the equation defining the x-position of a patch of water on a wave surface :

$$X(t) = (H/2)\cos(\Omega t) \qquad (1)$$

In the case of processing the intensity image of a standard marine radar, similar image intensity spectra result, but each radar frequency component must be scaled to some surface truth representation of the weave frequency spectrum using an emprical constant, a spectral Modulation Transfer Function. This has shown to be in error when environental conditions change (wind direction relative to wave direction, for example), and if the radar modulator ages with time and exhibits chaning output power. The coherent radar approach requires no such scaling, and is independent of such environmental factors. A patent based on this approach has been applice for by ISR and is pending, and an international provisional patent has also been filed.

IV. FREQUENCY SPECTRA AND H_m0

If one sums the spectral energy in the band about the shallow water dispersion relation for each of 32 windows, one derives an omni-directional freqeuency spectrum. A comparison of that derived from coherent radar data over 10 minutes, and the pressure array sensor at the FRF for two overlapping periods of 3-hr each is shown in Fig. 6 below.

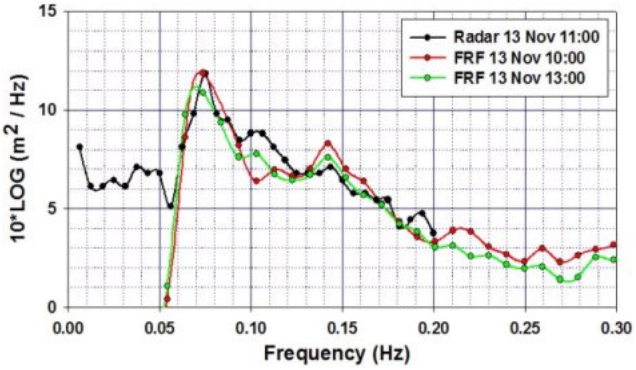

Figure 6. Frequency spectra from COHrad and FTF pressure array.

If one sums the energy from each spectral peak in the frequency spectrum above, one forms H_m0, a RMS waveheight estimate. During November of 2009, Hurricane Ida passed offshore of the FRF site and waves of 4-m were observed. Below are plotted the time series of H_m0 from the radar vs that from the FRF pressure sensor array.

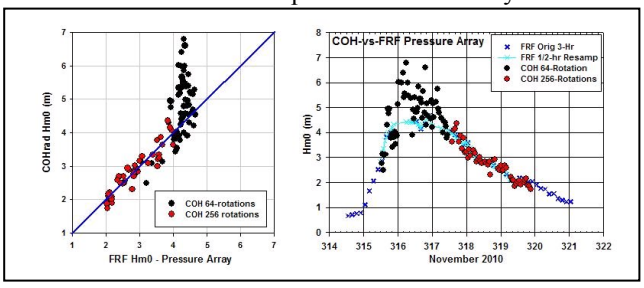

Figure 7. Hm0 time series from radar vs FRF pressure array compared.

The black circles represent very short times of collections, just 64 rotations covering ~2.5 minutes, enought for a single 3D-FFT analysis. As the winds subsided but the waves still being high, the collections were increased to 256 rotations, represented by the red circles. The agreement is quite good for these conditions and illumination into waves offshore of the pier end. It suggests that at least ten minutes of radar

data are required for a suitably stable Hm0 retrieval.

The CORrad was run simultaneously from the same location a frew meters away and processing that data in a similar fashion produced results for Hm0 as well. These are shown in Fig. 8 below.

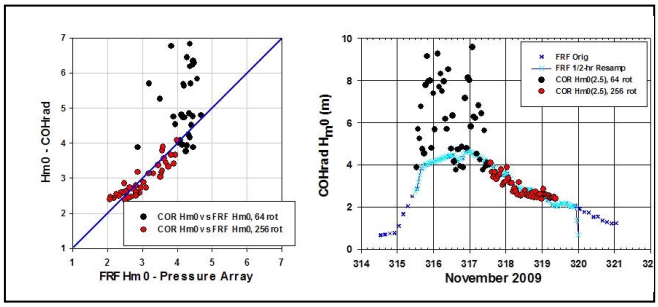

Figure 8. CORrad Hm0 vs FRF pressure array results

The results from the CORrad system are quite similar to those of the COHrad for the same period, and the need for more than 64 rotations of data are apparent here as well.

A third radar was operated at a different time in 2010, from a location on shore instead of the end of the pier. This is a scenario that is more likely for most potential applications. This was data from a CORrad as well, running over 512 rotations at twice the rotation rate of the COHrad, so covering the same 10-min or so time period. The height of the antenna was lower than that at the end of the pier, atop a 32' telescoping tower on ~3-m mean height behind the dune at the FRF site. They were collected at relatively short range, 384 m offshore, as onley 512 range samples were collected, and compared with FRF data from ~800 m offshore.

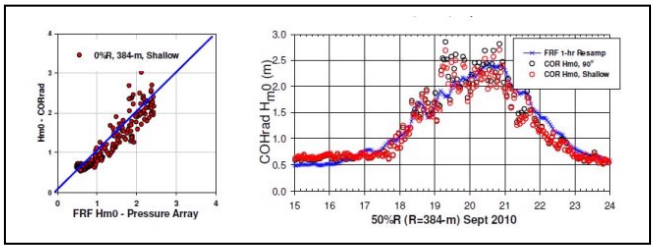

Figure 9. CORrad data from a shore site.

In this case, the results show the effect of the depth change with tidal cycle for the higher eave conditions, which was not accounted for. Nonetheless, the comparison is quite good for this shore side location.

V. RADIAL SURFACE CURRENTS

As discussed earlier, if one takes the mean of the sum of all radial velocity images, in the absence of severe shadowing of the wave troughs by wave crests for steep wave conditins and modest to high waves, one can derive radial surface currents from either type of radar discussed here. Fig. 10 below shows an example of 256 rotations summed for both radial velocity and magnitude images for the COHrad system during the Nov 2009 storm.

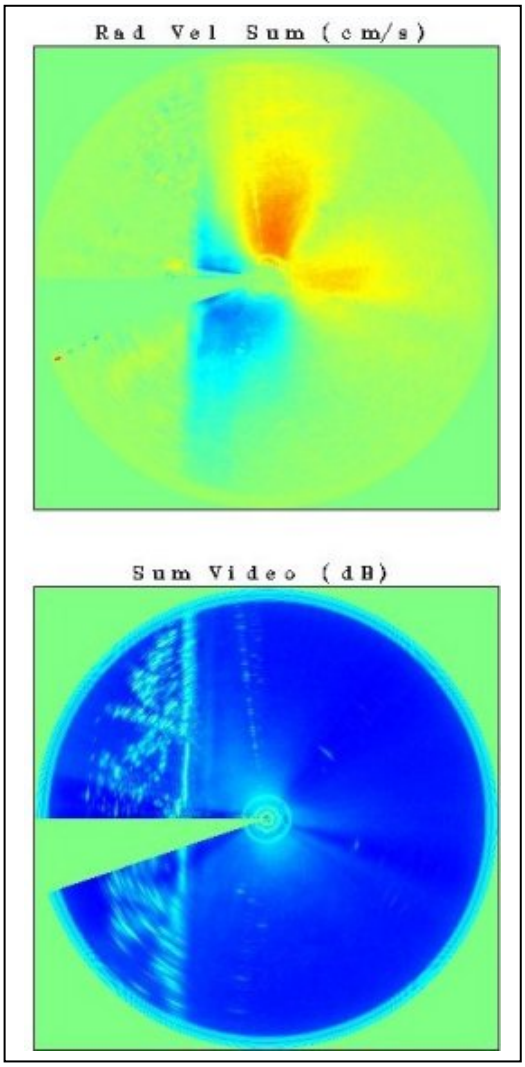

Figure 10. Summed radial velocity (top) and intenssity (bottom). The gap in the upper right quadrant of the redial velocity image is due to shadowing of the radar beam.

The maximum range extent in this case is about 700 m for the 1.5 km radar coverage (the pier is 600 m offshore). The drop off in radial velocity is thought to be due to the onset of shadowing, but has not been investigated thuroughly. Recent tests using a 19-m radar height was able to image currents out to 3-km range, so radial current measure is dependent on antenna height.

As the radar was turned during the experiment, it was difficult to make comparisons directly over surface truth currents from bottom mounted acoustic sensors that gave

vector values. Instead, we calculated currents over a range-azimuth ring, summing between 250-250 meters range extent, then over 10 adjacent azimuthal bearings of the 595 that were avialable. The maximum value in azimuth was determined to be a measure of maximum mean current. The acoustic Doppler vector currents were used to get a magnitude time history as well and these were compared. Because the maximum radar current magnitude was not necessarily at the same range-azimuth as the 5-m acoustic sensor, nor at the same depth, the comparisons should be taken with a grain of salt. The results of such a comparison is shown in Fig. 11.

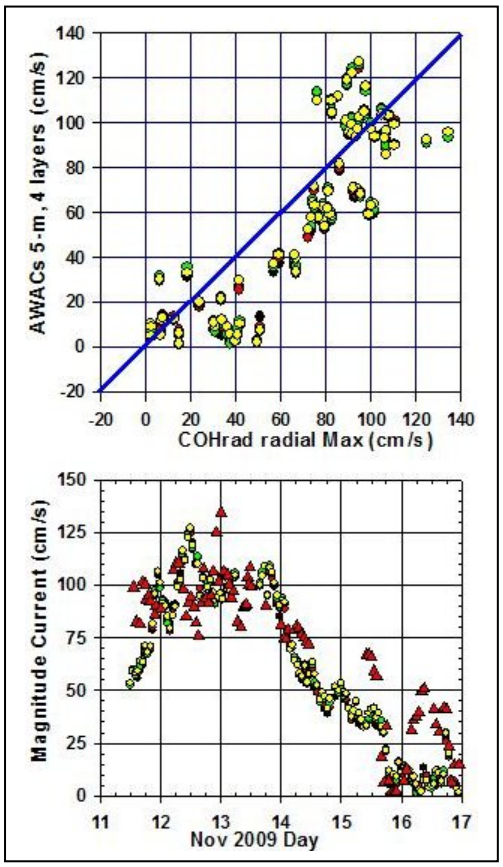

Figure 11. Time series of COHrad current magnitude (red triangles) and 3 acoustic depths near the surface, with scatter diagram comparison.

VIII. SUMMARY

We have demonstrated the use of a newly designed coherent marine radar to measure directional wave spectra and surface radial currents. Data were compared with surface truth instrumentation from the USACE Field Research Facility, both pressure array sensor data for wave height, and AWAC acoustic sensors for currents. Data from a coherent-on-receive radar that was run simultaneousl from the end of the pier at the FRF and compared favorably as well. For this location, currents along shore can be measured reasonably accurately for the modest radar height of roughly 11 m, as the radar is looking along the crests and troughs and does not suffer shadowing, even for modest to low radar height for this geometry. Looking offshore, the troughs would be shadowed by the crests for very steep waves, and the orbital wave velocity would not present a zero mean to the radar look. We found this to be the case for a shore based radar on another occasion, where the currents were in error due to crest orbital wave influences. For this case, the wave height analysis was still quite respectable. On more recent observations at other sites with radar heights ranging from 19 m to 26 m, no shadowing was encountered and long range currents could be measured accurately.

A pair of radars discussed here, placed of the order of 300 to 1,000 m apart, should be able to provide a vector map of surface currents at 3-m resolution. Such a method should be useful for detection of rip currents and riverene flow, in addition to currents in harbors for ship traffic application.

ACKNOLEDGEMENTS

We wish to acknowledge the data provided by the USACE FRF, in particular, to Kent Hathaway who extracted the data from historical records that allowed the comparisons to be made on a timely basis. ISR has a continuing Co-operative R&D Agreement with the FRF.

REFERENCES

[1] H. Dankert J. Horstmann, and W. Rosenthal, Ocean Wind Fields Retrieved from Radar-Image Sequences, J. Geophys. Res.. Vol. 108, 2005.

[2] I.R.Young, , W. Rosenthal, F. Ziemer, A three-dimensional analysis of marine radar images for the determination of ocean wave directionality and surface currents, JGR, **90**, C1, pp. 1049-1059, 1985.

[3] D.B. Trizna, "Errors in Bathymetric Retrievals using Linear Dispersion In 3D FFT Analysis of Marine Radar Ocean Wave Imagery," IEEE Trans. Geosciences and Remote Sensing, **39**, pp. 2465-2469, 2001.

[4] C.M. Senet, J. Seemann, F. Ziemer, An iterative technique to determine the near surface current velocity from time series of sea surface images, Oceans '97, Halifax, 1997.

[5] Dugan, J.P., H.H. Suzukawa, C.P. Forsythe, M.S. Farber, Ocean wave dispersions surface measured with airborne IR imaging system, IEEE Trans. Geosciences and Remote Sensing, **34**, pp. 1282-1284, 1996.

[6] Dugan, J.P., C.P. Forsythe, H.H. Suzukawa, M.S. Farber, Bathymetry estimates from long range airborne imaging systems, Proc. 4th Int. Conf. On Remote Sensing for Marine and Coastal Environments, Orlando FL, 1997.

[7] Stockdon, H.F., and R.A. Holman, Estimation of wave phase speed and nearshore bathymetry from video imagery, J. Geophysical Res., **105**, pp. 22,015-22,034, 2000.

[8] McGregor, J.A., E.M Poulter, M.J. Smith, Switching system for single antenna operation of an S-band FMCW radar, IEE Proc. –Radar, Sonar, Navig, Vol. 141, pp 241-248, 1994.